

---

This item was submitted to [Loughborough's Research Repository](#) by the author.  
Items in Figshare are protected by copyright, with all rights reserved, unless otherwise indicated.

## **Modification of the properties of D.C. magnetron sputtered magnetic thin films by self-bias**

PLEASE CITE THE PUBLISHED VERSION

PUBLISHER

© E.S. Warner

PUBLISHER STATEMENT

This work is made available according to the conditions of the Creative Commons Attribution-NonCommercial-NoDerivatives 4.0 International (CC BY-NC-ND 4.0) licence. Full details of this licence are available at: <https://creativecommons.org/licenses/by-nc-nd/4.0/>

LICENCE

CC BY-NC-ND 4.0

REPOSITORY RECORD

Warner, Edward S.. 2019. "Modification of the Properties of D.C. Magnetron Sputtered Magnetic Thin Films by Self-bias". figshare. <https://hdl.handle.net/2134/36439>.

LOUGHBOROUGH  
UNIVERSITY OF TECHNOLOGY  
LIBRARY

AUTHOR/FILING TITLE

WARNER, E S

ACCESSION/COPY NO.

036000209

VOL. NO.

CLASS MARK

LOAN COPY

30 JUN 1995

036000209 9





**MODIFICATION of the PROPERTIES of D.C. MAGNETRON SPUTTERED  
MAGNETIC THIN FILMS by SELF-BIAS**

**by E.S.Warner**

**A Master's Thesis Submitted in partial fulfilment of the  
requirements for the award of Master of Philosophy  
of the Loughborough University of Technology**

**September 1991**

**(c) by E.S.Warner 1991**

Loughborough University of Technology Library	
Date	Feb 92
Class	
Acc No.	036000209

W9921836

## ACKNOWLEDGEMENT

I wish to express my thanks to Dr.R.T.Giles, Dr.R.P.Howson, Dr.A.G.Spencer and Mr.E.M.Stenlake for the advice and motivation which they provided during this work and for their assistance in the final preparation of this thesis.

I am also grateful to all my colleagues at the Physics department whose help and encouragement contributed to my research.

## **ABSTRACT**

In this thesis a method to control the deposition process of D.C. magnetron sputtered magnetic thin films is described. A biased anode, situated in front of the magnetron, is used to alter the plasma characteristics which influence the film deposition process. The magnetic field configuration which results from biasing the anode leads to self-biasing at the film-substrate location. Control of this film self-bias voltage allows for controlled ion bombardment of the substrate.

The technique is investigated using Cobalt as the target material. With the given experimental configuration, self-bias voltages up to -40 V at the substrate location could be achieved. It is demonstrated that the use of self-bias and ensuing ion bombardment, during film growth at the substrate, influence the micro-structure and properties of the deposited films.

The micro-crystalline structure and coercivity of magnetron sputtered Cobalt films exhibited considerable variation with film self-bias. For increasing self-bias, the film coercivity attained a maximum value then decreased toward a value less than that of the unbiased case. It is found that the maximum value of coercivity coincides with the maximum film particle diameter. The films are found to consist essentially of single-domain particles, which are responsible for the observed magnetic properties of the films.

## **LIST of CONTENTS**

<b>1. INTRODUCTION</b>	<b>....1</b>
<b>2. THEORY of FILM DEPOSITION</b>	<b>....5</b>
2.1 Film Deposition	....5
2.1.1 Basics of Sputtering	....5
2.1.2 A Typical D.C. Sputtering System	....6
2.2 Atom Transport to the Substrate	...11
2.3 Film Growth Processes	...12
2.4 Plasma Diagnostic Techniques	...14
2.5 Substrate Heat Load	...18
2.6 Ferromagnetism and Internal Energy	...19
2.7 Small Particle Magnetism	...23
<b>3. TECHNIQUES - EXPERIMENTAL</b>	<b>...29</b>
3.1 Film Deposition	...29
3.2 Experimental Configuration	...30
3.3 Probe Measurements	...32
3.4 Substrate Heat Load	...33
3.5 Substrate Preparation	...34
3.6 Transmission Electron Microscopy	...34
3.7 Talystep Surface Profiler	...36
3.8 Energy Dispersive Analysis by X-Rays (EDAX)	...36
3.9 Magnetic Measurements	...37



<b>4. RESULTS</b>	<b>...39</b>
4.1 Self-Bias Voltage Calibration	...39
4.2 Heat Load	...39
4.3 Plasma Probe Measurements	...40
4.4 Diffraction Patterns and Bright-Field Images	...41
4.5 EDAX	...43
4.6 Magnetic Measurements	...44
4.7 Field Configuration - Magnetic	...44
4.8 Plasma Beam Configuration with Self-Bias	...45
<b>5. DISCUSSION of RESULTS</b>	<b>...47</b>
5.1 Film Composition	...47
5.2 Substrate Heat Load	...48
5.3 Analysis of Film Structure	...50
5.4 Self-Bias and Plasma Measurements	...55
5.5 Magnetic Measurements	...58
5.6 Film Stress	...61
<b>6. CONCLUSIONS</b>	<b>...64</b>

## LIST of SYMBOLS

<u>Quantity</u>	<u>Symbol</u>	<u>S.I. Unit</u>
Coercivity	$H_c$	$A m^{-1}$
Remanence	$M_r$	$A m^{-1}$
Magnetic Induction	$B$	$T$
Magnetic Field Strength	$H$	$A m^{-1}$
Magnetization	$M$	$A m^{-1}$
Permeability of Free Space	$\mu_o$	$H m^{-1}$
Boltzmann Constant	$k$	$JK^{-1}$
Electronic Charge	$q$	$C$
Electronic Mass	$m_e$	$kg$
Temperature	$T$	$K$
Melting Point	$T_m$	$K$
Energy	$E$	$eV$
Electric Field Strength	$E$	$V m^{-1}$
Voltage	$V$	$V$
Current	$I$	$A$
Current Density	$J$	$A m^{-2}$
Velocity	$v$	$ms^{-1}$
Time	$t$	$s$
Plasma Potential	$V_p$	$V$
Floating or Self-Bias Potential	$V_f$	$V$
Pressure	$p$	$Pa$
Radius	$r$	$m$
Drift Velocity	$u_d$	$ms^{-1}$
Debye Length	$\lambda_d$	$m$
Number Density	$n$	$m^{-3}$

Mean Free Path	$\lambda$	m
Mass Density	$\rho$	$\text{kgm}^{-3}$
Specific Heat Capacity	$c_p$	$\text{Jkg}^{-1}\text{K}^{-1}$
Thermal Conductivity	$k_t$	$\text{Wm}^{-1}\text{K}^{-1}$

The Sommerfeld Convention for Magnetic Quantities in S.I. Units is Adopted:

$$\vec{B} = \mu_0(\vec{H} + \vec{M})$$

Notation for Subscripted Quantities:

i	Ion
e	Electron
$i_s$	Ion Value at Sheath Boundary
$e_s$	Electron Value at Sheath Boundary

## 1. INTRODUCTION

Magnetic thin films have been produced by various processes such as chemical (1,2), electro and electroless (3,4) and ion plating (5), vacuum evaporation (6,7) and sputtering (8,9). The latter option is the most attractive proposition in terms of the achievable film properties, however, it is an expensive technique due to the vacuum conditions required during film deposition. During sputtering, the film material is transformed into the vapour phase by a mechanical (momentum exchange) process. The implication of this is that almost any material may be considered as a potential film coating. Moreover, sputtering can produce films at high rates (deposition rates of  $1\text{-}10\text{ nm s}^{-1}$ ) with reproducible, controllable properties that are uniform over large areas. The material is deposited with energies corresponding to temperatures of a few thousand degrees celsius. This provides for good film adhesion and crystallinity.

Magnetic thin films ( $<0.5\text{ }\mu\text{m}$  thick) have many uses: as recording media for high density digital recording due to their relatively large induction (10), as logic elements in electronics and memory elements in computers, and as security tags. In the first instance, the necessary conditions are that the film should have a high coercivity ( $H_c$ ) and as high a squareness of hysteresis loop as possible (1,10,11). Squareness ( $S$ ) is defined as the ratio of the remanence ( $M_r$ ) to saturation ( $M_s$ ), i.e.  $S = 1$  ideally. In the other cases a high squareness is also desirable. However, a small coercivity is required due to the limiting size of the detection systems.

In this study the microstructure and magnetic properties of planar magnetron sputtered pure Cobalt films are investigated. Cobalt metal, a ferromagnetic material, has a large value of saturation ( $1.42\text{ }10^6\text{ Am}^{-1}$ ) and its hexagonal close-packed structure a high uniaxial anisotropy ( $K_u = 45\text{ }10^4\text{ Jm}^{-3}$  at

298 K). These factors suggest the possibility of a high coercivity for Cobalt in the form of a thin film.

The magnetic properties of thin films depend on film structure, which in turn depend on film growth. It has been shown (12) that bias voltages applied to the substrate during deposition can have a considerable influence on the structure of the deposited films. The effects of bias may manifest themselves by altering the plasma characteristics, by thermal effects and by re-sputtering. In metals, the combined effects of these phenomena are known to influence the film crystallinity (13). It is known that ion bombardment during thin film growth produces changes in nucleation characteristics, in morphology, in composition, in crystallinity and in film stress (14). The conventional method of depositing a film whose properties are modified by a flux of high energy particles is ion plating (5,15). However, the cost of equipment and associated technical problems are a serious drawback to the process.

In the case of direct application of bias to the substrate, a potential sheath is created in front of the substrate. The changes in structure and properties of the magnetic thin films associated with bias, are assumed to originate from increased bombarding ion energy and preferential re-sputtering of Oxygen at moderate bias (-50 V), (16,17).

In this study an alternative method of influencing film deposition is considered. Any isolated conductor immersed in a plasma will become negatively charged due to the greater mobility of electrons over other species. The conductor will achieve a fixed potential, the floating potential or self-bias voltage, relative to the container walls as ground. This occurs when the ion flux to the conductor just balances the electron flux reduced by electrostatic repulsion. This is the condition of net zero

current to the conductor. A space charge forms in front of the conductor of polarity such as to accelerate ions. The kinetic energy of ions impinging on the conductor is approximately the charge per ion multiplied by the self-bias voltage. Thus, controlling the self-bias voltage enables control of the energy of incident ion flux. Although, in the majority of cases, fast neutral atoms sputtered from the target represent the majority species bombarding the substrate, the ion flux has been demonstrated to have a considerable effect on film growth and structure (18,19).

In this study, the microstructure and magnetic properties of planar magnetron sputtered Cobalt films 500-600 nm thick are investigated. The deposition process is modified by altering the plasma characteristics, which is achieved by varying the potential of an electrode immersed in the plasma thereby altering the substrate self-bias voltage.

## 1. REFERENCES

- 1) Fisher R.D. and Chilton W.H., J.Electrochem Soc., 109 (1962), p.485.
- 2) Judge J.S., Morrison J.R. and Speliotis D.E., J.Electrochem Soc., 113 (1966), p.547.
- 3) Tsu I., Plating, 48 (1961), p.207.
- 4) Sallo J.S. and Olsen K.H., J.Appl. Phys. Suppl., 32 (1961), p.2035.
- 5) Takao M. and Tasaki A., IEEE Trans. Magn. MAG-12, (1976), p.82.
- 6). Speliotis D.E., Bate G., Alstad J.K. and Morrison J.R., J.Appl. Phys., 36 (1965), p.972.
- 7) Odagiri M., Kumieda T., Fujita T., Shinohara K., Iijima Y. and Tomago A., IECE Japan Tech. Rep., MR-78-3 (1979).
- 8) Kay E., J.Appl. Phys. Suppl., 32 (1961), p.995.
- 9) Rogalla D., IEEE Trans. Magn., MAG-5 (1969), p.901.
- 10) Lazzari J.P., Melnick I. and Randet D., IEEE Trans. Magn., MAG-3 (1967), p.205.
- 11) Bate G., IEEE Trans. Magn., MAG-1 (1965), p.193.
- 12) Maissel L. and Glang R., Handbook of Thin Film Technology, McGraw Hill, New York (1970), Chap.4.
- 13) Mattox D.M. and Kominiak G.J., J.Vac. Sci. Technol., 9 (1972), p.528.
- 14) Movchan B.A. and Demischin V.A., Phys. Met. Metallogr., (USSR) 28 (1969), p.83.
- 15) Mattox D.M., Electrochem Tech., 2 (1964), p.295.
- 16) Hammer W.N. and Ahn K.Y., J.Vac. Sci. Technol., 17 (1980), p.3169.
- 17) Okmoshi M., Okhata R., Inoue K., Honda S. and Kusuda T., Jpn.J. Appl. Phys., 19 (1980), p.1807.
- 18) Teer D.G., Tribology Intl., 8 (1975), p247.
- 19) Matthews A. and Teer D.G., Thin Solid Films, 72 (1980), p.541.

## 2. THEORY of FILM DEPOSITION

The films in this study were produced by D.C. magnetron sputtering of a planar circular source in a vacuum chamber. Sputtering is a process where energetic particles bombard a surface and eject material through momentum transfer processes. The film material, called the target, is placed in a vacuum chamber along with substrates and evacuated to  $133 \mu\text{Pa}$  or so. Inert gas ions constitute the bombarding species.

Bombardment is initiated by back filling the chamber with inert gas to a pressure less than  $13 \text{ mPa}$  and striking an electric discharge. This is a low pressure glow discharge and the ionized gas is a plasma. The target constitutes the negative electrode of the discharge to facilitate ion bombardment and plasma formation. In a magnetron system, crossed electric and magnetic fields are employed to accelerate and confine the electrons that ionize the working gas. The electric field accelerates ions into the target, these ions 'knockout' target atoms which constitute the film. The flux is intercepted by substrates positioned in front of the target. Moreover, secondary electrons emitted by the target are used to make the process self-sustaining (1).

Film production involves three processes: sputtering of the target atoms, the transport of these atoms to the substrate and film growth from these atoms.

### 2.1 FILM DEPOSITION

#### 2.1.1 Basics of Sputtering

As previously stated, sputtering involves a momentum transfer process. In sputtering, the bombarding particle transfers its kinetic energy to the



target atoms . Target atoms that attain sufficient kinetic energy to overcome the local binding forces are ejected through the target surface. The process may be viewed on an atomic level and compared to collision between hard elastic spheres.

Consider a particle of mass  $m_j$  and velocity  $v_j$  incident at an angle  $\phi$  to the line of centres with a particle of mass  $m_t$  initially at rest, Fig.1. It can be shown (1) that the fraction of incident kinetic energy transferred to the target atom is:

$$\frac{E_t}{E_i} = \frac{4 m_j m_t \cos^2 \phi}{(m_j + m_t)^2}$$

This indicates that maximum energy transfer occurs when  $m_j = m_t$ , for a head-on collision. This is the ideal case. However, more generally, the target atom is driven into the target by momentum exchange. The ejection of a sputtered particle ensues only when the direction of the initial momentum alters by more than  $90^\circ$  due to a sequence of collisions.

The sputtering of a single element target is defined as the number of target atoms ejected per incident particle. It is dependent upon the nature of the target and its surface profile, and on the nature of the incident particles, their energy and angle of incidence (2). Fig.2. illustrates the variation of sputtering yield for Argon ions at normal angles of incidence for various metals. The sputtered energy distribution is approximately Maxwellian with a most probable energy of 10 eV (2).

### 2.1.2 A Typical D.C. Sputtering System

The target is fabricated from the material to be sputtered. It is made to be the cathode of an electrical circuit, Fig.3., with a large negative D.C

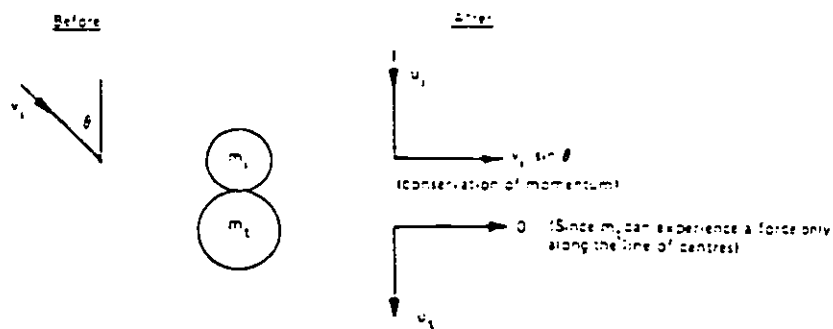


Fig1 Velocity components before and after an elastic collision

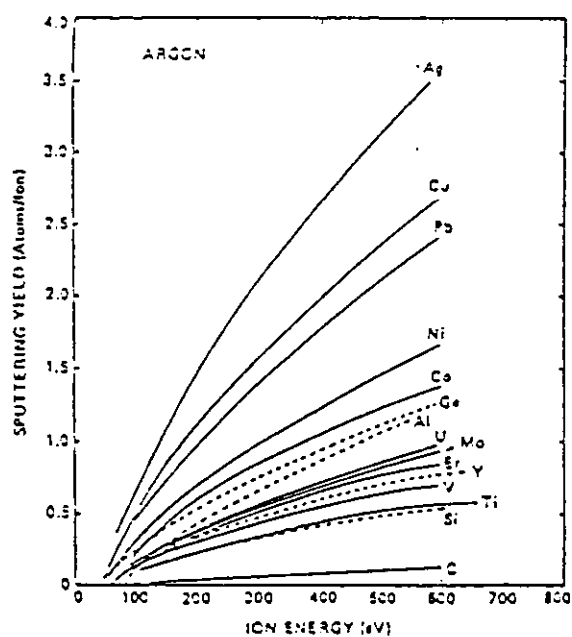


Fig.2 Variation of sputtering yield with ion energy for  $\text{Ar}^+$  ions at normal incidence.

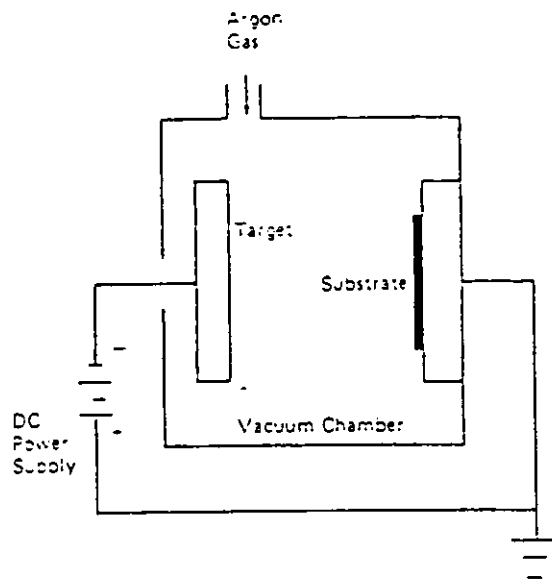
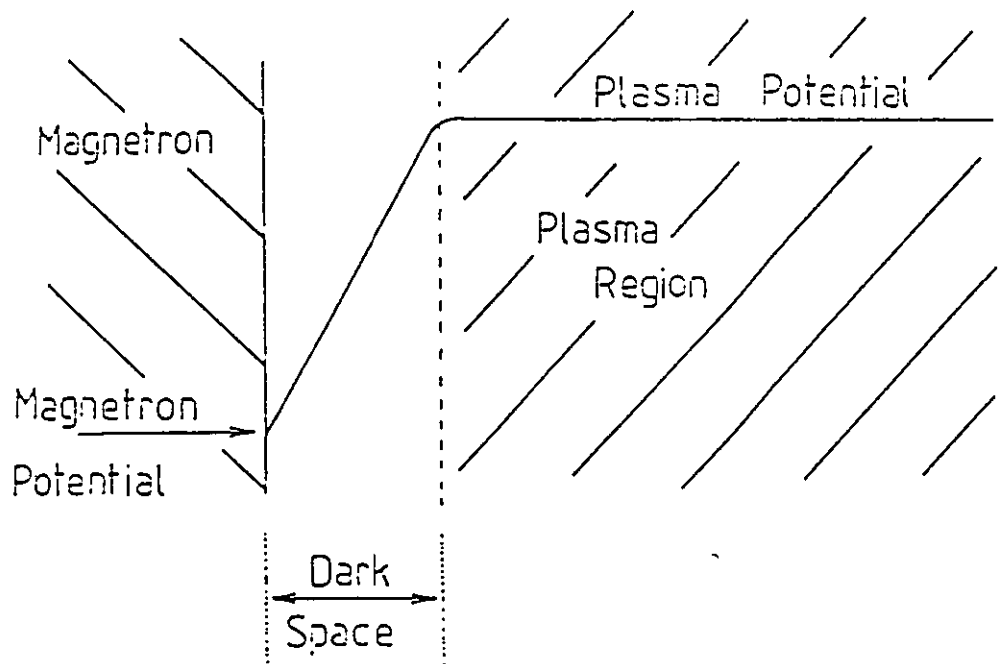


Fig.3 Schematic of a d.c. sputtering system.

Fig.4 The Plasma and Dark Space above the Magnetron Surface



voltage applied to it. The substrate, upon which the sputtered material is to be deposited, is located on a grounded anode several centimetres from the target. Working gas, usually inert such as Argon or Krypton, is admitted to the chamber. Inert gases are used chiefly because they are relatively cheap, readily available, mass compatible and unreactive. Electrons are accelerated by the electric field, and by collisions with gas atoms, produce ions and electrons. This constitutes a low pressure glow discharge, as previously explained. The electric field accelerates the ions to the target to induce sputtering and secondary electron emission. The electrons tend toward the anode. Thus a current flows. To sustain the discharge, the rate of production of ions in the plasma volume must be sufficient to balance the fluxes of electrons and ions to the electrode and chamber wall surfaces. Secondary electron emission from the target is utilized to achieve this (1).

The D.C voltage required to maintain the current through the system is a function of the gas pressure and electron mean free path. The rate of film deposition depends on the ion flux to the target. The magnitude of sputtering depends on the sputtering yield. This is dependent on ion energy (4), see Fig.4, and thus to applied voltage which is responsible for the sheath voltage at the target.

For a magnetron in operation, a plasma exists above the target surface. The plasma attains a positive potential, relative to the chamber walls as ground. This occurs because electrons escape from the plasma to the walls faster than ions due to their greater mobility. A steady state value of potential is achieved because loss of electrons from the plasma leave it positive and prevents escape of further electrons, i.e. the process is self-limiting. The magnetron has a large negative potential and the plasma a positive potential. Clearly a region or voltage sheath, a sort of transition region, exists between the two, Fig.4. It is across this region

that the applied potential exists. Above the target surface the electric field is such as to repel electrons, thus the region is a 'dark space'(5).

A magnetron uses crossed electric and magnetic fields to increase ionization in the plasma by confining electrons above the target surface. This accounts for the relatively small thickness of the dark space, usually 1 mm or less. The path of an electron under the influence of such fields may be determined by solving the so called Lorentz equation:

$$\frac{d\bar{v}}{dt} = \frac{q}{m_e} (\bar{E} + \bar{v} \times \bar{B})$$

(the bar denotes vectors)

For mutually perpendicular uniform electric and magnetic fields the situation above the target surface is depicted in Figs.5,6. The general trajectory for a given initial velocity may be determined by solving the equations of motion:  $F_x = q(E - v_z B)$ ,  $F_z = m_z \ddot{z} = qv_x B$ . However, there is an alternative approach. A charge of velocity  $v_z = E/B$  experiences no force in the x-direction, this means it effectively travels in a zero x-field. Now if  $v_z \neq E/B$ , a non-zero x-field exists. If we let  $v_z = u_z + E/B$ , then our equations of motion are:  $F_x = qu_z B$ ,  $F_z = qv_x B$ . The resulting motion, as in Fig.7., is seen to be that of a cycloid. It is a combination of uniform circular motion and uniform linear drift velocity in the same plane. The radius of circular motion is given by:  $r = (m_e v / qB)$ , where the components of  $v$  are  $u_z$  and  $v_x$ .

In planar D.C. magnetron sputtering the applied potential is usually in the range -300 V to -600 V, with magnetic fields of 0.011 T to 0.11 T. For a dark space thickness of 0.5 mm, and taking the electric field as the negative of the potential gradient, the radius of circular motion is given

Fig. 5 Electron Motion in crossed  $\vec{E}$  and  $\vec{B}$  Fields

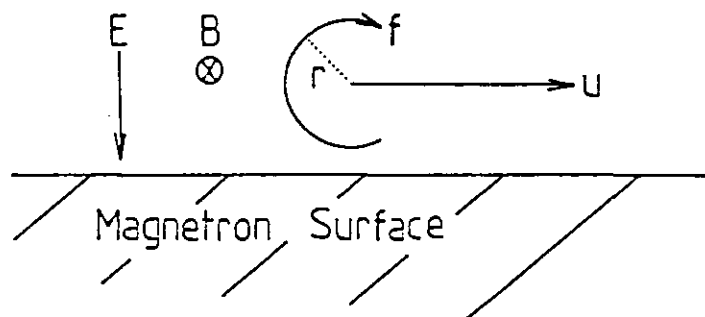
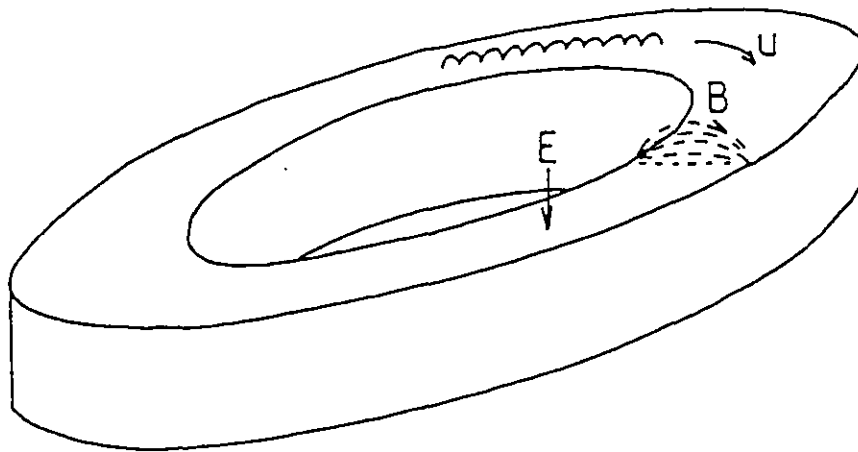


Fig. 6 The Closed Electron Drift Path required for Magnetron operation



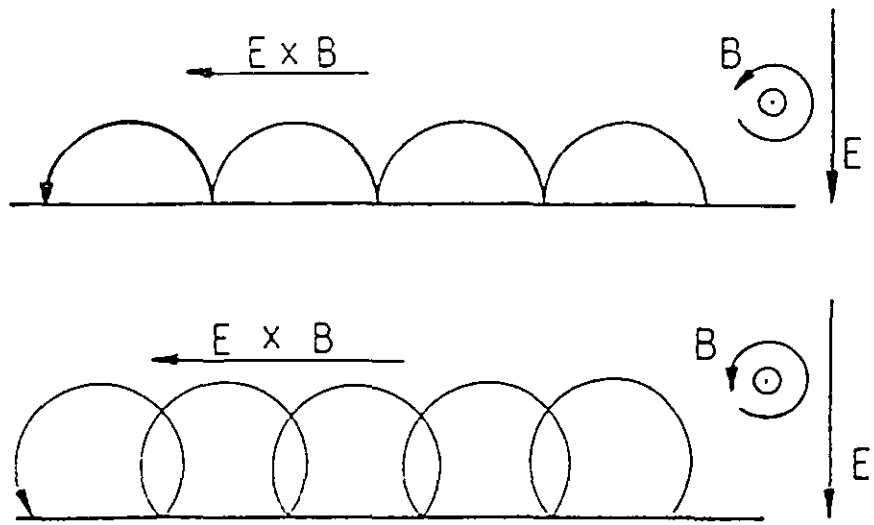


Fig.7 Electron motion in an  $E \times B$  field.

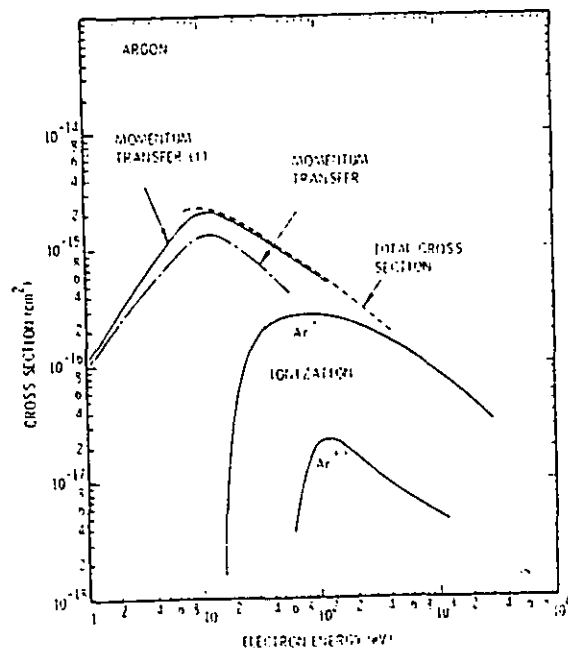


Fig.8 Collision cross sections for Electrons in Argon gas.

by (21):  $r = (Em_e)/(qB^2)$ , where  $0.7 \text{ mm} \leq r \leq 4 \text{ mm}$ . This implies that an electron may traverse the dark space and leave the region of electric field.

Upon leaving this region, the electron energy is a constant and the radius of curvature of its path reduced. For a 500 eV electron in a magnetic field of 0.05 T, the radius is approximately 1.5 mm. If the electron remains confined in the electric field region, the frequency of circular motion may be estimated by:  $f = (qB)/2m_e \approx 4 \text{ GHz}$ , and the drift velocity  $u_d = E/B$  is  $\approx 2 \cdot 10^7 \text{ ms}^{-1}$ .

As stated the drift velocity must be perpendicular to the mutually perpendicular electric and magnetic fields. This implies that electrons will escape from the magnetron. To prevent this, and to ensure a stable discharge, a circular magnetron was employed to provide closed electron drift paths.

To produce ionizing collisions, the electrons in the magnetron must travel distances at least equal to that of the mean free path. For a chamber pressure of about 0.4 Pa, the number density of atoms (from the equation of state for an ideal gas) is around  $10^{20}$  atoms per  $\text{m}^3$ . The average collision cross-section of electrons in Argon gas for the given conditions, from Fig.8., is around  $10^{-20} \text{ m}^2$ . The mean free path is of the order 1 m. The previously described motion of electrons indicates that the electrons will drift approximately half the total distance traversed. The circular magnetron employed in this instance, with a drift path of 0.1 m diameter, implies that electrons must be confined for at least three traversals of the loop.

In the circular magnetron employed here, a magnetic field oriented across the target was imposed by means of magnets, Fig.9., so as to inhibit electron motion tangential to the drift loop. The field configuration



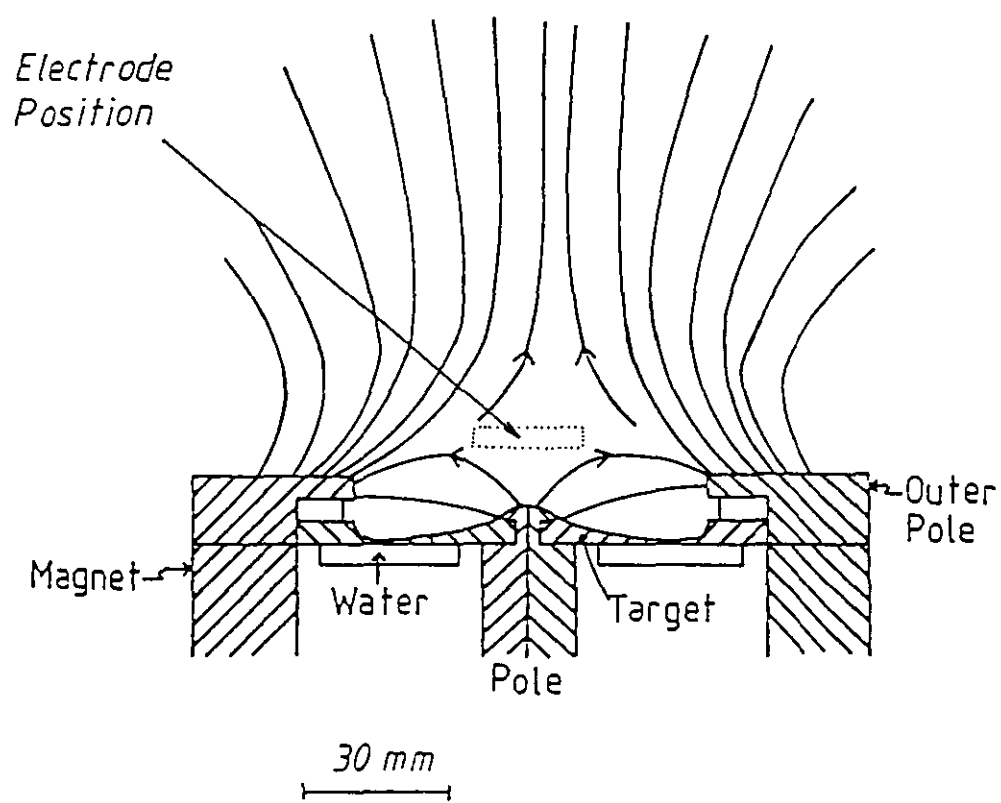


Fig.9 Magnetron Configuration.

implies that the electric and magnetic fields are perpendicular over the central region. Thus there must be an electric field component parallel to the magnetic field. Electrons accelerated by the electric field will acquire a velocity component  $v'$  parallel to the magnetic field. The component will thus be unaffected by the magnetic field ( $\vec{v}' \times \vec{B} = 0$ ). The electron will travel along the field line away from the target.

The use of ferromagnetic target materials presents difficulties in that they disturb the magnetic flux above the target. Figs.10,11 illustrate the problem and its solution. The poles of the magnet are situated in front of the target in order to create fringing fields. The purpose of this design is to ensure that the flux crosses the space between the target and the poles.

It is seen that the effective electron confinement can be effected by judicious use of magnetic fields. Ions produced as a result of ionization due to electron confinement are accelerated through the applied potential and sputter material from the target. Ion bombardment of the target leads to phenomena such as momentum transfer to target atoms, secondary electron emission, ion trapping in the target and target heating (6).

Bombarding ion energy, due to acceleration through the applied potential, is in the range 300-1000 eV. A large fraction of the incident power, 70%-90%, is dissipated as heat in the target (7). The target must therefore be cooled, usually by a system involving cold water circulation. The fraction of incident power transferred to the sputtered material leads to sputtered particle energies of 10-100 eV.

For a metallic target, the sputtered material is in atomic form. For sputtering using Argon as the working gas, sputtered atom velocities for

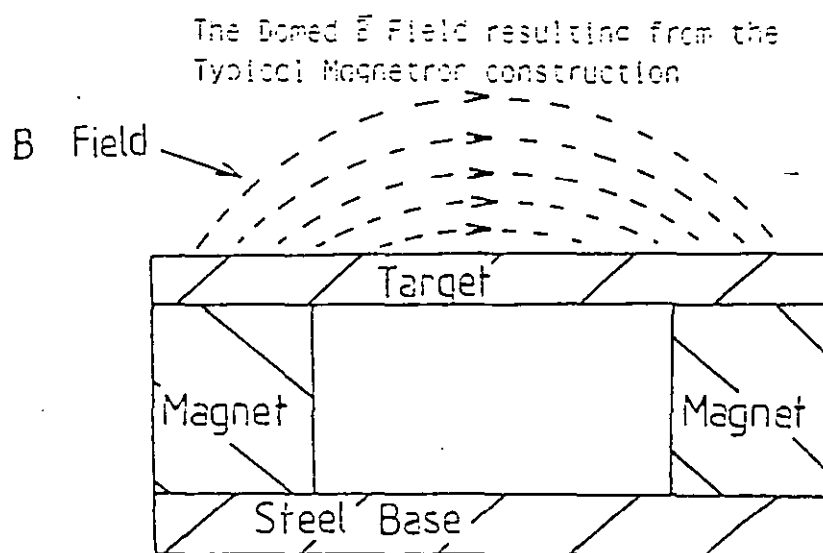
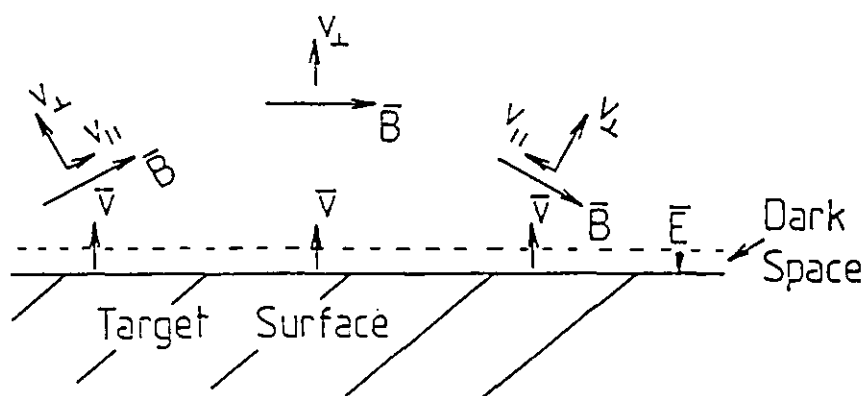


Fig.10 Electron velocities across the dome field due to the component of  $\vec{E}$  parallel to  $\vec{B}$



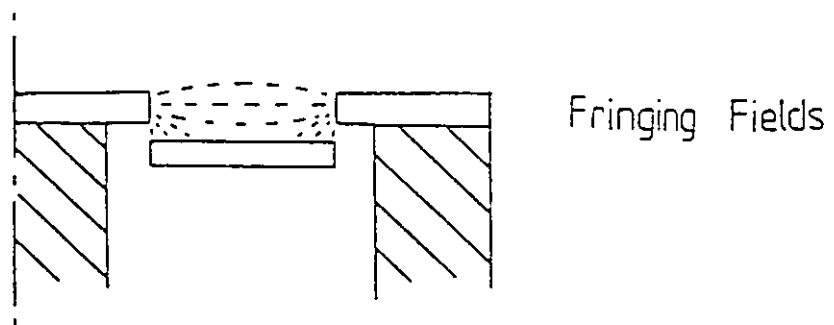
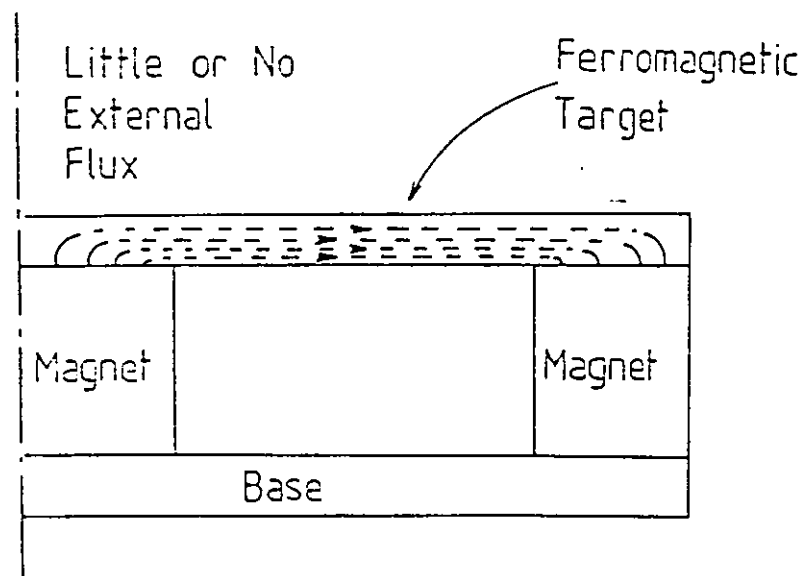


Fig.11 The Effect of a Ferromagnetic Target on the Magnetic Field Configuration.

metals have been found to be in the range  $3\text{-}6 \text{ kms}^{-1}$  (8). The sputtered atom energy depends directly on the mass and for the transition metals, such as Cobalt, is approximately 10 eV. It has been shown (9) that the energy distribution exhibits a tail to high energies, however, the majority of atoms possess energies of a few eV.

## 2.2 ATOM TRANSPORT to the SUBSTRATE

The sputtered atoms ejected from the target possess energies of a few eV. The energy of atoms incident on the substrate is directly influenced by the number of collisions suffered during transport to the substrate. Moreover, these collisions will affect the angular distributions of atoms incident on the substrate. It has been demonstrated that sputtered atom energy and angle of incidence affect the structure of the deposited films (10,11).

The sputtered atom energy is considerably more than that of the gas atoms in the chamber (normally 1 eV or less). Thermalization of the sputtered species due to collisions with gas atoms will alter the energy distribution. Thermalization is determined by the product of the chamber gas pressure  $p$  and the target to substrate distance  $d$ . The number of collisions is proportional to  $d$  and inversely proportional to the mean free path, which is inversely proportional to  $p$ . Hence, this implies that the number of collisions is proportional to the product  $pd$ . As previously discussed, the most efficient energy exchange should occur for atoms of compatible mass (the hard sphere model). For this model, collision cross-sections for atoms of atomic number greater than 20 is approximately constant (12). Fig.12. shows thermalization of Argon ions in Argon gas, from (35). Due to the mass difference, thermalization of Cobalt atoms in Argon gas may be expected to require a  $pd$  product in excess of the equivalent in Fig.9.

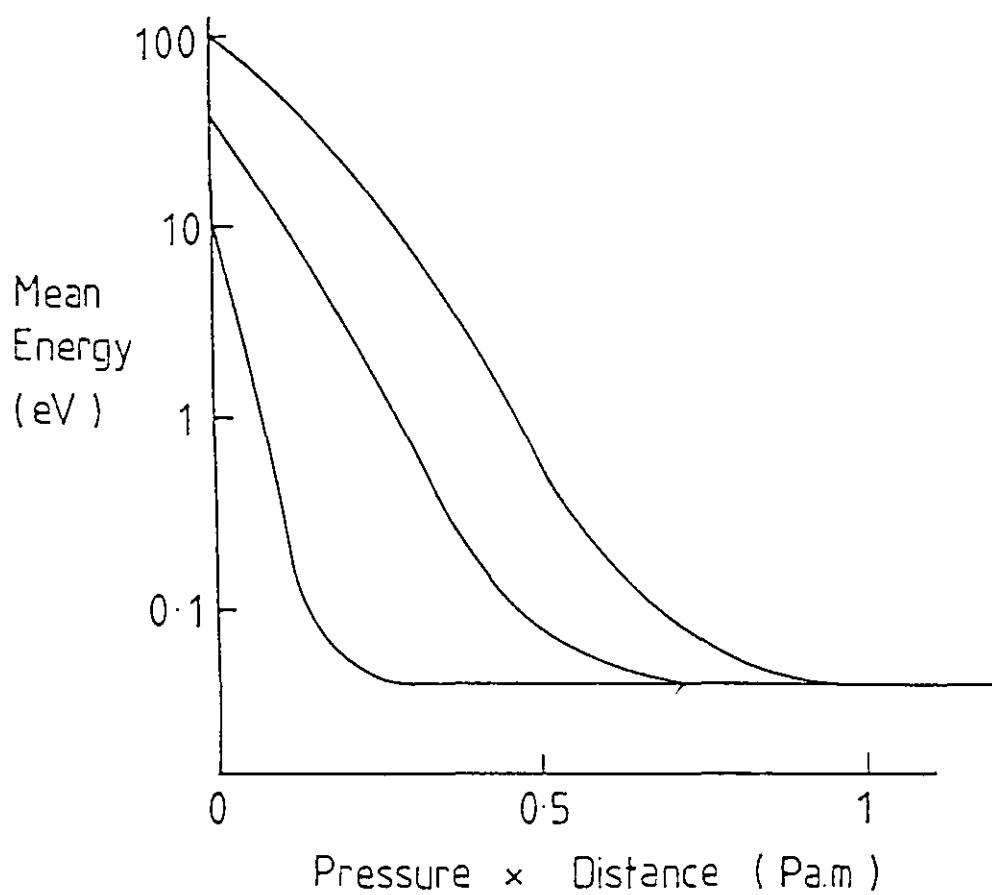


Fig.12 Thermalisation of fast Argon atoms into Argon.

### 2.3 FILM GROWTH PROCESSES

The nucleation and growth of thin films on surfaces is but little understood, and is still an area of intense research effort. Of particular interest to thin film growth is the interfacial region between the film and the substrate, and the film structural development once a continuous film has formed on the substrate.

The initial arrival of atoms at the substrate and their motion on it is collectively known as condensation. Atoms incident on the surface can undergo reflection, adsorption for a finite time or adsorption and stick permanently. The probability of reflection is relatively low from a practical point of view. The incident atoms will generally transfer a sufficient amount of their kinetic energy to ensure that they become loosely bonded to the substrate. These adatoms have mobility over the surface, a diffusion process, during which they may exchange energy with substrate atoms or other resident particles. These processes continue until they are desorbed by evaporation or re-sputtering, or become trapped at low energy sites (nucleation sites) on the substrate, Fig.13.

The nature of the substrate and its surface can greatly influence the initial growth of a film, particularly in relation to the film crystal size, orientation and phase. The substrate cleanliness, structure and defect density can affect the nucleation site density. The nucleation site density depends on the incident atom to substrate bond strength and the incident atom interactions. The fraction of incident atoms that adhere to the substrate depends on the atom energy and the substrate temperature (13).

From the above considerations, it can be seen that the parameters relating to the initial layer growth are quite considerable. A more complete review

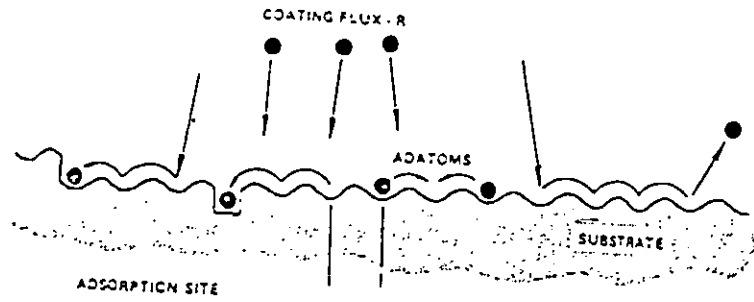
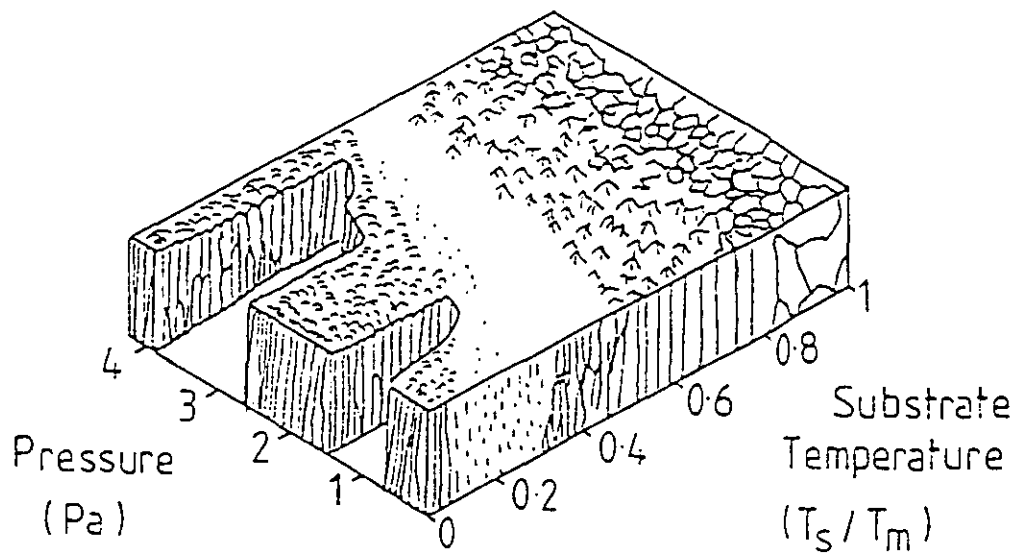


Fig.13 Schematic illustration of condensation processes that occur during film growth.

Fig.14 The effects of pressure and substrate temperature on the film structure





may be found in (2). The incident atoms condense in groups at low energy sites and coalesce to form islands. These islands coalesce to form a continuous film. This may be established by observing the electrical and optical properties which exhibit a marked change when the islands coalesce (16). For metals this leads to a continuous layer at a thickness of 5-15 nm.

The stage when a continuous layer forms indicates the point where the substrate has no direct effect on the film growth. Atoms are now incident on a surface which is of the same nature. The processes are now determined by three parameters. Firstly, the absorption energy between adatoms and the developing film, secondly, the surface diffusion energy to transfer an adatom to an adjacent absorption site and thirdly, the binding energy between the film atoms. Structured films may now develop, for instance, the adatoms possess surface mobility and have a high probability of being trapped at low energy sites. Thus a preferred crystal orientation may develop as a result. Crystals at these sites grow at the expense of their neighbours, a sort of 'survival of the fittest' (17). Moreover, energetic particle bombardment, such as ion bombardment, can substantially influence the nucleation and growth processes. This may occur due to removal of impurity atoms, the creation of nucleation sites and by influencing adatom mobility (14). All these effects have significant consequences for the deposition and growth of magnetic thin films. It is a well established fact that the magnetic properties of such films are dependent on their structure.

The evolution of microstructure is governed by adatom diffusion over the surface of the same species, as previously indicated. However, evolution and growth of such structure may also be influenced by bulk diffusion and atomic shadowing (17). At elevated temperatures, atoms incorporated into the film may change location in the lattice structure by bulk diffusion

processes. The shadowing effect is a result of an interaction between the non-uniformity of the growing film surface and the incident directions of the sputtered atoms.

The melting point of the film material is an important parameter, as it can be related to adatom binding and activation energies. This indicates that the ratio of the substrate temperature to the film melting point,  $T/T_m$ , may be used to determine which of the growth mechanisms prevails. This leads to the concept of zone models, the first of which was proposed by Movchan and Demischin, Fig.14. Thornton (5) proposed a modification to this model, in the absence of ion bombardment, to account for the effect of the working gas on the film structure. This zone model implies that the ratio  $T/T_m$  is proportional to adatom mobility. At low ratios, a columnar structure interspersed with voids develops (20). For increasing ratios, the adatom mobility increases. This leads to increased crystal sizes thus precluding the columnar formation.

## 2.4 PLASMA DIAGNOSTIC TECHNIQUES

Plasma measurements can provide information relating to the processes that affect the performance of the glow discharge sputtering devices. A glow discharge plasma can be imagined as a region of relatively low temperature gas in which the degree of ionization is determined by the presence of energetic electrons.

Electrostatic (Langmuir) probes provide an useful means with which to investigate sputtering types of plasma (22,23). The current-voltage (I-V) characteristic curves of probes, whose size is small enough to limit perturbation of the plasma, are measured. Probe techniques and analyses originate from the work of Langmuir and Mott-Smith (24). Detailed analyses

of the theory of Langmuir probes can be found in (22,23).

A plasma consists of three species of particles. These are ions, electrons and neutrals. On average, ion and electron densities are equal and this density is called the plasma density. This density is usually less than that of the neutral particles. An electrostatically isolated conductor immersed in a plasma is subjected to the random ion and electron fluxes. The electrons possess a greater mobility than the ions and the conductor thus acquires a net negative charge, and hence a negative potential with respect to the plasma.

The electron flux decreases due to electrostatic repulsion but the isolated conductor will continue to charge negatively until the ion flux just balances the reduced electron flux. Apart from perturbations (Debye Shielding), a plasma is field free and equipotential. This is termed the plasma potential  $V_p$ . The potential associated with the isolated conductor is termed the floating potential or self-bias voltage  $V_f$ , with the walls of the containing vessel taken as ground. The polarity and magnitude of  $V_f$  is such as to repel electrons and to equalize the ion and electron fluxes. It corresponds to the point of zero net current on the I-V curve.

To facilitate analysis of a plasma, the following assumptions are made. They relate to the case of a low pressure plasma such as a gas discharge below 13 mPa:

- 1) Electron and ion densities are equal.
- 2). Electron and ion mean free paths are much larger than the probe radius.
- 3) Electron temperature is much larger than the ion temperature.

4) The probe radius is much larger than the Debye length.

5) There is a Maxwellian distribution of electron and ion velocities.

A positive space charge or sheath develops in front of an isolated conductor immersed in a plasma. The potential variation in this region, an exponential decrease, is characterized by a decay length  $\lambda_d$  called the Debye length given by:

$$\lambda_d = \sqrt{(kT_e)/n}$$

When a conductor is biased, the sheath adjusts rapidly to screen out most of the voltage. However, a small potential gradient, termed the pre-sheath or quasi-neutral region, extends into the plasma. This is illustrated in Fig.15. The electric field in this region accelerates ions, thus the ion density at the outer sheath boundary is larger than that due to thermal diffusion alone. The potential at this point  $V_o$  has been found to be (25):

$$V_o = (kT_e)/2q = 1/2\phi$$

for all types of probes. This implies that ion sheath formation occurs only if  $V \gg V_o$ .

The ion velocity and current density at the outer sheath boundary,  $V_{is}$  and  $J_{is}$ , for a low pressure plasma where  $T_e \gg T_i$  is given by (26):

$$v_{is} = \sqrt{(2qV_o/m_i)} = \sqrt{(kT_e/m_i)}$$

$$J_{is} = (qn_{is}v_{is})$$

Assuming equal densities of ions and electrons in the quasi-neutral region, and a Maxwellian distribution for electron velocities:

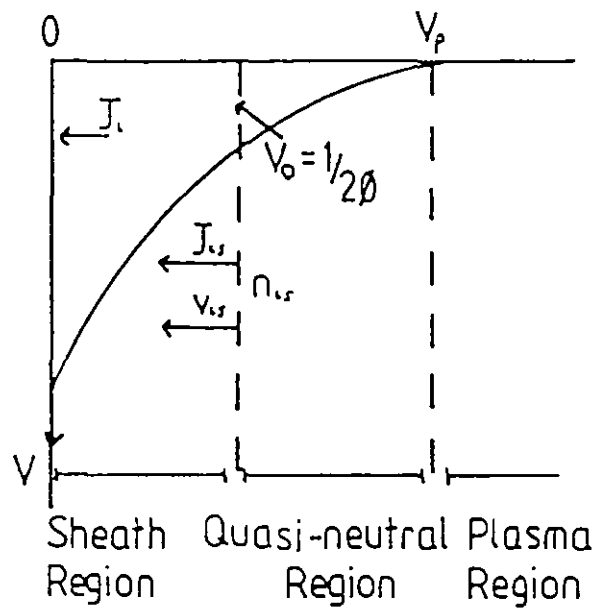


Fig.15 Potential distribution around a probe in the region of ion current.

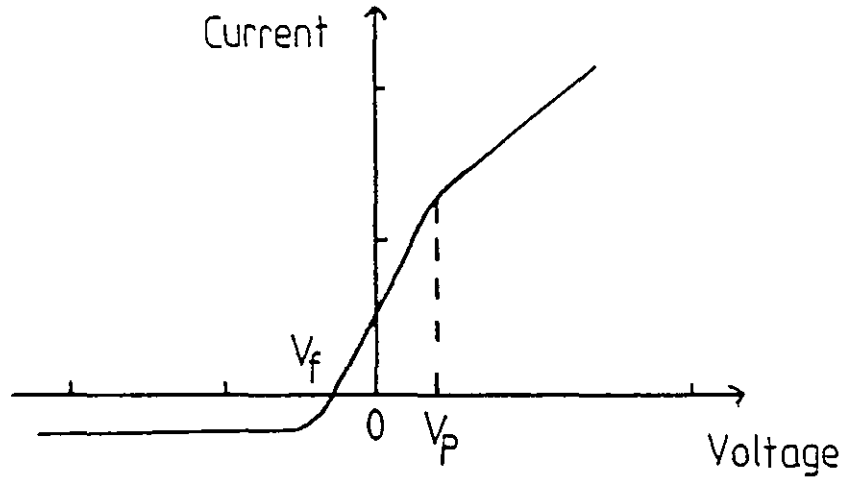


Fig.16 Typical Probe Characteristic.

$$n_{is} \approx n_{es} = n_e \exp(-\Phi/2\phi) = n_e \exp(-1/2)$$

If the surface area of the outer sheath boundary  $S'$  is assumed equal to the probe surface area  $S$ , then:

$$J_i = (S'/S) J_{is} \approx J_{is}$$

$$J_e = qn_e \sqrt{(kT_e/2\pi m_e)}$$

$$J_e = 0.657 J_i \sqrt{(m_i/m_e)}$$

The most notable feature of these equations is the deduction that the saturation ion current density  $J_i$  is determined by the electron temperature  $T_e$ .

Fig.16 illustrates the conventional form of probe characteristic. When the probe voltage is large and negative, the probe is strongly negative with respect to the plasma. The surrounding sheath prevents even the most energetic electrons reaching it, thus the probe current is due entirely to ions. As this potential becomes less negative, fast electrons can surmount the retarding field so the net probe current is reduced. The point for net zero current to the probe corresponds to  $V_f$ . It is negative with respect to the plasma since electron mobility exceeds that of ions. As the probe voltage decreases further, the probe current (which is now of opposite polarity) increases due to the decrease in the field opposing the electrons. When the probe reaches the plasma potential  $V_p$  the electrons experience an accelerating field. The conditions governing electron current alter, indicated by the region after the knee of the curve. The plasma conditions determine the effects in this region.

A plot of the natural logarithm of probe current versus that of probe

voltage, in the electron retarding region of the I-V curve, will have a slope of  $(q/kT_e)$ . Measurement of the ion saturation current and knowledge of  $T_e$  enable the various current densities to be calculated. The difference in potential between the probe and the surrounding plasma, when the net probe current is zero, can be found by equating the expressions for the ion and electron saturation currents. This yields:

$$V_f = (kT_e/2q) \ln \left[ (m_i/2\pi x^2 m_e) \right]$$

where  $x = \exp(-1/2)$ .

## 2.5 SUBSTRATE HEAT LOAD

In the experimental configuration, the substrates are in contact with a plasma and are bombarded by sputtered atoms and plasma species. Energy flux measurements are used to determine the contributions to substrate heating. It has been shown that substrate temperature is an important parameter for film growth (19).

It is known (27) that energy transfer processes in the discharges used in sputtering lead to substrate heating. Measurements reveal, that on commencement of sputtering, there is an initial rapid rise in substrate temperature with a subsequent approach to equilibrium after a few minutes.

The most direct method to measure the effective flux at the substrate is to measure the rate of rise of temperature of a thermally massive object which possesses a good thermal conductivity. These conditions are necessary so that one may neglect any thermal gradients caused by poor thermal conductivity, and so that the temperature after a reasonable amount of time is low enough that one may neglect radiative cooling.

For a plate of mass  $m$  and specific heat capacity  $c_p$ :

$$p_i = mc_p(dT/dt)$$

where  $p_i$  is the incident power and  $dT/dt$  the time rate of change of temperature of the plate. If the power is incident on one face only, the incident flux becomes:

$$\Phi = \rho dc_p(dT/dt)$$

where  $\rho$  is the mass density and  $d$  the thickness of the plate. This relation may be considered adequate provided the thermally massive object approximates to a linear, homogeneous, isotropic medium whose dimension in the direction of incident power is such that the medium may be considered to always be at equilibrium, i.e. thin. Thus,  $\Phi$  may be considered as the effective absorbed power density at the substrate position. A normalized parameter of  $\Phi$  divided by the input power flux may be determined to compare the heating effects at the substrate in a sputtering system under various conditions.

## 2.6 FERROMAGNETISM and INTERNAL ENERGY

Cobalt is classed as a ferromagnetic material because it possesses a large positive magnetic susceptibility and may be magnetized by a weak magnetic field. This type of material exhibits hysteresis, i.e. the magnetic flux through the material depends not only on the presence of a magnetic field but also on the previous magnetic history of the material. When the material is magnetically cycled energy dissipation occurs during the cycle.

The energy in a ferromagnet consists of several components: exchange energy, anisotropy energy, magnetostatic or demagnetizing energy, domain wall energy and if external magnetic fields are applied, Zeeman energies. For any physical system to achieve a stable equilibrium condition, the energy of the



system must be minimized. Note, a ferromagnetic material cycled around a hysteresis loop is not in its minimum energy state. In such a material the minimization of energy leads to the existence of domains. A domain is a region of crystalline matter of volume  $10^{-8}$  to  $10^{-12} \text{ m}^3$ , which contains atoms whose magnetic moments are aligned in the same direction. It is thus a magnetically saturated region and behaves like a magnet with its own magnetic axis and moment. Domain formation depends upon the existence of exchange forces between atoms in a ferromagnet. Domains are separated by finite boundaries called walls, within which the spin orientation changes from one to the other by rotating about an axis perpendicular to the plane of the wall. Ferromagnetism is a cooperative phenomenon. It is due to the alignment of atomic spins and associated magnetic moments, and is expressed as the magnetization per unit volume  $\bar{M}$ . In Cobalt, ferromagnetic behaviour is believed to be due to the uncompensated spins of the 3d electrons.

### 2.6.1 Magnetic Energies

To determine the properties of a ferromagnetic sample a magnetic field  $H$  is applied and the behaviour of  $\bar{M}$  is studied. When a field  $H$  is applied to a sample of magnetization  $\bar{M}$ , there is a torque  $\bar{M} \times H$  experienced by  $\bar{M}$ . This torque attempts to align  $\bar{M}$  with  $H$ . The external field energy is:

$$E_{\text{ext}} = -\mu_0 H \cdot \bar{M}$$

This is a minimum when the two entities are parallel.

If at any point in the sample  $\bar{M}$  is no longer continuous, then magnetic poles are created. These poles are associated with an internal field that opposes magnetization. The magnetostatic energy due to these poles is:

$$E_{\text{mag}} = -1/2 \mu_0 H_{\text{mag}} \cdot \bar{M}$$

The factor 1/2 occurs because a self-energy is concerned.

The properties of a sample may depend upon the direction in the sample along which they are measured, i.e. the sample exhibits anisotropy. This may be envisaged as the direction  $\vec{M}$  takes with respect to a set of co-ordinate axes fixed in the sample. If the direction cosines of  $\vec{M}$  are  $x_1, x_2, x_3$  then the anisotropy energy is:

$$E_k = K_u f(x_1, x_2, x_3)$$

$K_u$  is the anisotropy constant, and is some function of the direction of  $\vec{M}$  takes in the sample.  $E_k$  may attain minimum and maximum values depending upon the direction of  $\vec{M}$ . These directions are termed easy and hard respectively. In general,  $E_k$  is dependent on the sense of  $\vec{M}$  so these directions are called easy and hard axes.

Spin alignment is due to a quantum effect, the exchange force. The consequence of this effect is to prevent deviation of  $\vec{M}$  from alignment. If a deviation occurs, then the exchange energy is given by:

$$E_{ex} = A/M^2 |\nabla M|^2$$

where  $\nabla$  is the grad operator,  $A$  is the exchange constant of the material.

Thus the total energy of the sample is the sum of these contributions. Each component is, in general, a function of sample position and of the direction of  $\vec{M}$  at that position. For any given material, any of these may or may not be present. Similarly, under various conditions, certain of the components may be the dominating factor.

### 2.6.2 Magnetic Anisotropy

This may be taken to mean the dependence of the internal energy on the

direction of spontaneous magnetization. Several components may contribute simultaneously to constitute the magnetic anisotropy energy.

The geometric shape of the sample leads to the creation of a demagnetizing field due to the presence of magnetic poles on the surface of the magnetized sample. The amount of demagnetization is dependent on the shape and magnitude of the magnetization. For regularly shaped geometries, e.g. ellipsoidal, the demagnetization field is:

$$H_{\text{mag}} = N_x M_x + N_y M_y + N_z M_z$$

where the subscripted N's are the demagnetizing factors for directions in the sample.

If the sample is a single crystal, a magneto-crystalline anisotropy exists due to spin-orbit coupling. The energy  $E_k$  depends upon the direction of  $\vec{M}$  with respect to the crystal axes.

If  $\phi_0$  is the angle between the easy axis and  $\vec{M}$  and  $K_u$  is the anisotropy constant, then an anisotropy of the form  $\sin^2 \phi_0$  is known as an uniaxial anisotropy. There are two states of lowest energy ( $\phi_0 = 0, \pi$ ) and  $E_k = K_u \sin^2 \phi_0$ . Uniaxial anisotropy is often characterized by an effective field  $H_k = 2K_u / \mu_0 M$  (28).

Magnetostriction is that process occurring when the shape of a ferromagnetic sample changes during magnetization. The ratio of change in length to original length,  $\delta l/l$ , is small ( $\approx 10^{-5}$  to  $10^{-6}$ ). The strain due to magnetostriction varies with increase of magnetic field, ultimately reaching a saturation value. For a uniform stress  $\sigma$  applied to a randomly oriented polycrystalline sample, the energy of the strained state is  $E_k = 3/2 \sin^2 \phi_0$ , where  $\phi_0$  is the angle between  $\vec{M}$  and the direction of stress.

## 2.7 SMALL PARTICLE MAGNETISM

The domains in a ferromagnetic material are separated by boundaries or walls of finite thickness. These walls may move in the presence of an applied magnetic field, causing the bulk magnetization to change accordingly. The wall thickness depends on the energy contributions present in the film.

Namely, magnetostatic energy which is a minimum for an infinitely thick wall, and the crystalline anisotropy energy which is a minimum for abrupt transitions between domains. Hence, if the particle size becomes small as compared to the normal wall thickness, energy considerations preclude domain formation. The particle will thus remain as a single domain particle.

Magnetization of the particle may now be envisaged as rotation of the magnetization vector under the action of an applied field. Rotation of the vector is opposed by the anisotropic components of the sample.

It is convenient, when considering the magnetic behaviour, to investigate the case of complete saturation of  $\vec{M}$  in a single domain, i.e.  $\vec{M}$  remains coherent indefinitely.  $\vec{M}$  is directed uniformly at some angle  $\phi_0$  with respect to the easy axis at all points in the film. If a magnetic field is applied at an angle  $\beta$  to the easy axis,  $\vec{M}$  can be rotated out of the easy axis. If  $H$  and  $K_u$  are known, the orientation of  $\vec{M}$  can be determined.

The total energy is the sum of the contributions due to anisotropy energy  $E_k$  and magnetostatic energy  $E_{\text{mag}}$ , so:

$$E_{\text{tot}} = K_u \sin^2 \phi_0 - \mu_0 H M \cos(\beta + \phi_0)$$

The minimum energy condition is obtained upon differentiation  $dE_{\text{tot}}/d\phi_0 = 0$ . The angle  $\phi_0$  is determined by the equilibrium between opposing torques. If the applied field is parallel to the easy axis then  $\beta = 0$  and the first

derivative is 0 at  $\phi_0 = 0$ . For this to be a minimum, the second derivative must be positive. This yields the condition  $\mu_0 H M + 2K_u > 0$ . For a field applied anti-parallel to  $\vec{M}$  then the energy minima will be retained until a critical field is exceeded. This is the anisotropy field  $H_k$  given by  $2K_u/\mu_0 M$ . The orientation of  $\vec{M}$  will now change to the position corresponding to the new energy minimum with  $\vec{M}$  parallel to the applied field. This yields a square hysteresis loop of coercivity  $2K_u/\mu_0 M$ .

The above described model is that due to Stoner and Wohlfarth (28) for a single domain particle. In general, it predicts coercivities in excess of that measured in actual samples. The model ignores the effect of particle anisotropy. The discrepancy in coercivity may be accounted for by particle interactions and incoherent rotation (of the vector  $\vec{M}$ ).

The magnetostatic energy depends upon the shape anisotropy, which leads to pole separation distribution. If the internal energy of the system can be reduced by non-coherent rotation of  $\vec{M}$  this process will be favoured.

The 'chain and spheres' model of Jacobs and Bean (29) was the first successful attempt to account for this effect. Moreover, increasing the film packing fraction may reduce the coercivity due to particle interactions.

Magnetocrystalline anisotropy is due to spin-orbit coupling. Atoms interact via exchange forces, such forces may vary with relative atomic position. Hence, as the magnetization vector rotates, so the internal energy may vary (30). This form of anisotropy is related to the crystal structure of the sample. In Cobalt, for example, it may be approximated by  $K_u \sin^2 \phi_0$ . The magnetic field acting on a particle is the sum of that applied field and that due to the surrounding particles. Rotation will occur when this interaction is sufficient to prevail over the exchange forces.

No theoretical model exists to predict the hysteresis loop of an assembly of interacting single domain particles. Moreover, in the case of sputtered films other factors also need to be taken into consideration. Films often contain particles exhibiting a wide range in size due to growth mechanisms, interactions between such particles are difficult to model.

The behaviour of small magnetic particles depends upon their sizes. As the size decreases, behaviour changes from multi-domain to single domain. Further size reduction results in transition from single domain to superparamagnetic particles.

Superparamagnetism is the name given to the phenomenon when the magnetization of a collection of particles can change state unhindered. The particles appear to lose all remanence and coercivity but with high magnetization. An energy barrier exists to magnetization reversal which is proportional to particle volume  $V$ . When this energy corresponds to that of the order of thermal fluctuations, the phenomenon occurs. The critical volume for this behaviour is well defined and is given by (31):

$$V = (25kT/K_u).$$

For Cobalt this yields a critical diameter of 7.6 nm for particles to exhibit superparamagnetic behaviour. It has been shown in theory and by experiment that an assembly of single domain and superparamagnetic particles exhibits a reduced coercivity as compared to the single domain case only (32,33).

The critical size below which a particle becomes single domain may be estimated from (34), critical diameter  $L_c$  given as:

$$L_c = \frac{2\sqrt{2} \sigma w}{(\mu_0 M^2/6 - K_u/2)}$$

$w$  is the wall energy per unit area  $\approx 3 \cdot 10^{-3} \text{ Jm}^{-2}$ . For Cobalt this gives  $L_c \approx 42 \text{ nm}$ . Hence the maximum coercivity should be seen in the particle size range 8 nm to 42 nm, with the maximum in coercivity occurring near the limit of this range.

## 2. REFERENCES

- 1) Chapman B., in Glow Discharge Processes, Wiley and Sons (1980), Chap.1.
- 2) Thornton J.A., Semiconductor Materials and Process Technologies, Noyes Publication (1984).
- 3) Bohm D., in The Characteristics of Electrical Discharges in Magnetic Fields, McGraw Hill (1949).
- 4) Vossen J.L. and Cuomo J.J, in Thin Film Processes, Academic Press, New York (1978), p.11.
- 5) Thornton J.A., in Deposition Technologies for Films and Coatings, Noyes (1982).
- 6) Martin P.J., J.Mat. Sci., 21 (1986), p.1-25.
- 7) Hill R.J., in Physical Vapour Deposition, Aircotemesal Berkeley, California (1970).
- 8) Wehner G.K. and Andersson G.S., in Handbook of Thin Film Technology, ed. Maissel L. and Glang R., McGraw Hill, New York (1970).
- 9) Stuart R.V. and Wehner G.K., Trans. 9<sup>th</sup> Nat.Vac.Symp., (1962).
- 10) Hoffman D.W. and Thornton J.A., J.Vac. Sci. Technol., 20 (1982) 3.
- 11) Barber Z.H. and Somekh R.E., Vacuum, 34 (1984), p.1011.
- 12) Motohiro T. et. al., IPAT'83, Proc. Int. Ion Eng. Cong., Kyoto, Japan (1983).
- 13) Lewis B. and Andersson J.C., Nucleation and Growth of Thin Films, Academic Press, New York (1978).
- 14) Thornton J.A., Ann. Rev. Matter Sci., 7 (1977), p.239.
- 15) Howard J.K., J.Vac. Sci. Technol., A(4), 1, (1986), p.1-13.
- 16) Valkonnen E., IPAT'85, CEP Consultants, Edinburgh (1985).
- 17) Futamoto M. et. al., Jap. J. Appl. Phys., 24 (1985), p.6.
- 18) Brophy J.H., Rose M. and Wulff J., The Structure and Properties of Materials, Vol.2, Wiley Press, New York (1964).
- 19) Movchan B.A. and Demischin V.A., Phys. Met. Metallogr., 28 (1969).



- 20) Dirks A.G. and Leamy H.G., Thin Solid Films, 47 (1977).
- 21) Duffin W.J., in Electricity and Magnetism, McGraw Hill(1980).
- 22) Chen F.F, in Plasma Diagnostic Techniques, ed. Huddleston R.H. and Leonard S.L., Academic Press, New York (1965).
- 23) Swift J.D. and Schwar M.J.R., in Electrical Probes for Plasma Diagnostics, Iliffe Books, London (1971).
- 24) Langmuir I. and Mott-Smith H., Gen. Elec. Rev., 27 (1924), p.449 and 538, 616, 762, 810.
- 25) Allen J.E., Boyd R.L.F. and Reynolds P., Proc. Phys. Soc., London, 70B, (1957), p.297.
- 26) Chen S.L. and Sekiguchi T., J.Appl. Phys., 36 (1965), p.2363.
- 27) Ball D.J., J.Appl. Phys., 43, 7, (1972), p.3047.
- 28) Stoner E.C. and Wohlfarth E.P., Phil.R.Trans. Soc., A240, (1948), p599.
- 29) Jacobs I.S. and Bean C.P., J.Appl. Phys., 27 (1956), p.1948.
- 30) Van Vleck J.H., Phys. Rev., 52 (1937), p.1178.
- 31) Cullity B.D.,Introduction to Magnetic Materials, Addison-Wesley, London (1952).
- 32) Meikljohn W.H., Rev. Mod. Phys., 25 (1953), p.302.
- 33) Kneller E.F. and Luborsky F.E., J.Appl. Phys., 34 (1963), p.656.
- 34) Kittel C., Phys. Rev., 70 (1946), p.965.
- 35) Somekh R.E., Ibid., p.987.

### 3. TECHNIQUES

#### 3.1 FILM DEPOSITION

The films studied in this extract were produced by sputtering from a planar D.C. magnetron source. The cylindrical deposition chamber measured 0.5 m in diameter by 0.65 m in height. The chamber was pumped through a vent of diameter 0.2 m. Initial evacuation, down to approximately 27 Pa, was achieved through the use of a rotary pump. An oil diffusion pump was then employed to evacuate down to a working vacuum of approximately 3 mPa.

Argon comprised the working gas, of purity 99.9995%, and at approximately 0.4 Pa deposition pressure. The pumping speed for Argon was measured for the oil diffusion pump to be 240 litres per second at 0.7 Pa chamber pressure. If it is assumed that impurity pumping speed corresponds approximately to that of Argon, then the impurities in Argon had a partial pressure of  $10^{-6}$  Pa. This is two orders of magnitude below the chamber base pressure. It was assumed that outgassing contributed largely to the chamber base pressure.

The chamber base pressure corresponds, from the equation of state for an ideal gas at 300 K, to a chamber population of around  $8 \times 10^{16}$  atoms. This condition corresponds to a dynamic balance between outgassing from the chamber walls and the pump rate.

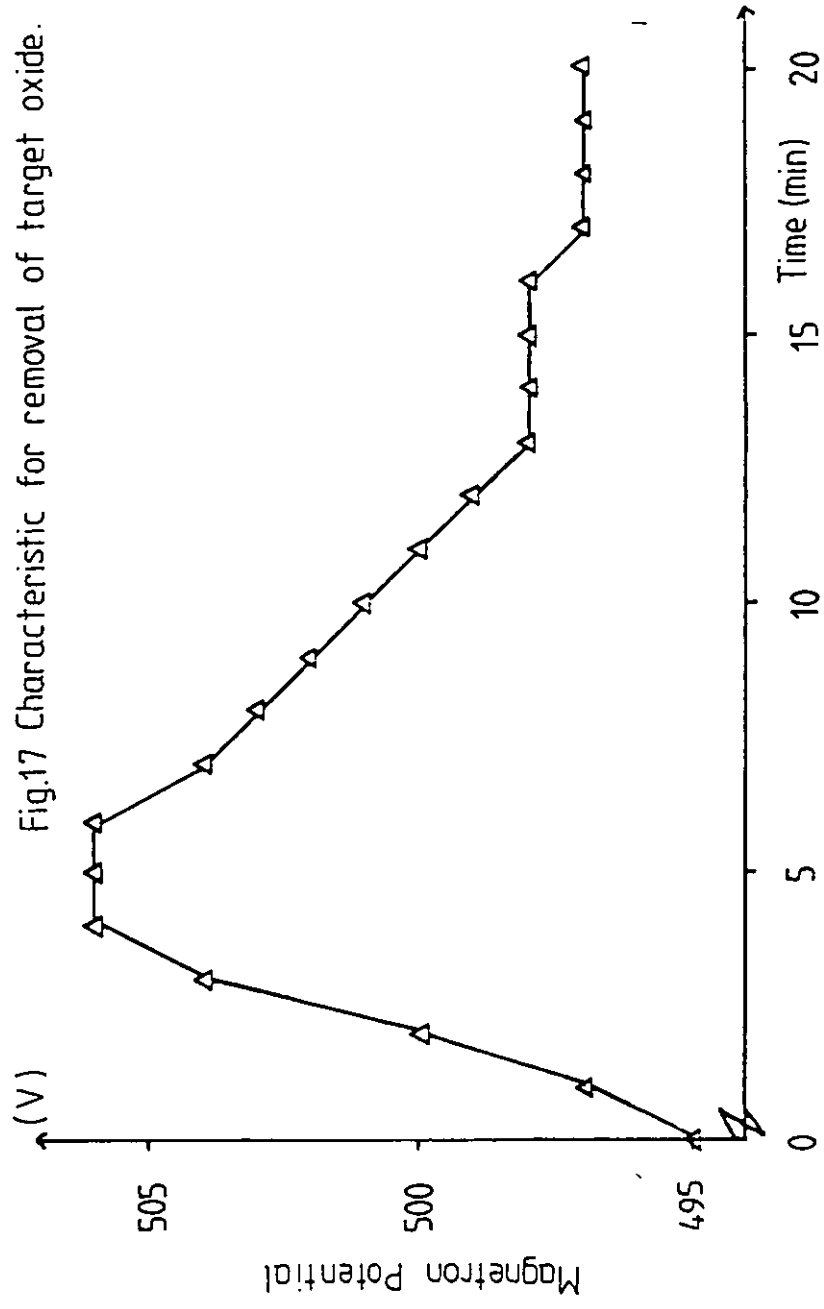
The area of Cobalt film deposited was around 75 mm  $\times$  22 mm of thickness 550 nm. This corresponds to approximately  $8 \times 10^{19}$  atoms. Inclusion of gaseous impurities in the film should not have drastically altered the impurity partial pressure.

The working gas pressure of 0.4 Pa was selected as a compromise between several factors. These were the relation between electron collision cross-section and mean free path in Argon gas and the pressure required to maintain the discharge, the dependence of thermalization of Argon ions in Argon gas and gas pressure, and the vacuum pump stall pressure. The film deposition rate was determined as follows. Glass slides were weighed before and after a known deposition period. Knowing the applied power, the deposition rate in ( $\text{kg m}^{-2} \text{W}^{-1} \text{s}^{-1}$ ) can be found. The film deposition rate corresponded approximately to  $1.5 \text{ nms}^{-1}$ , corresponding to an atomic adhesion rate of  $1.4 \cdot 10^{20} \text{ atoms m}^{-2} \text{s}^{-1}$ . Assuming an impurity partial pressure of  $3 \cdot 10^{-3} \text{ Pa}$  and using the equation of state for an ideal gas, the impurity bombardment was around  $5 \cdot 10^{19} \text{ atoms m}^{-2} \text{s}^{-1}$ . The adhesion rate appears to exceed the impurity bombardment rate by an order of magnitude. However, the impurity level in the film should be checked as it is known to influence film growth and properties (1).

An additional source of impurity was the Cobalt target. Oxidation, when exposed to air, can occur. Thus the target was sputter cleaned, with the substrates shielded, for some 15 to 20 minutes prior to film deposition. Fig.17. illustrates the target voltage against time, removal of any oxides etc. are complete when voltage stabilization occurs.

### 3.2 EXPERIMENTAL CONFIGURATION

The experimental configuration inside the vacuum chamber is illustrated in Fig.18. The target is a circular disc of Cobalt, purity 99.995%, 77 mm in diameter and 1 mm thick. The copper anode is 30 mm in diameter, water cooled and mounted 30 mm from the target along the target axis. An Aluminium shield 380 mm by 300 mm, with a window 95 mm by 40 mm, is mounted 80 mm from the target along the axis. An Aluminium electrode surrounding



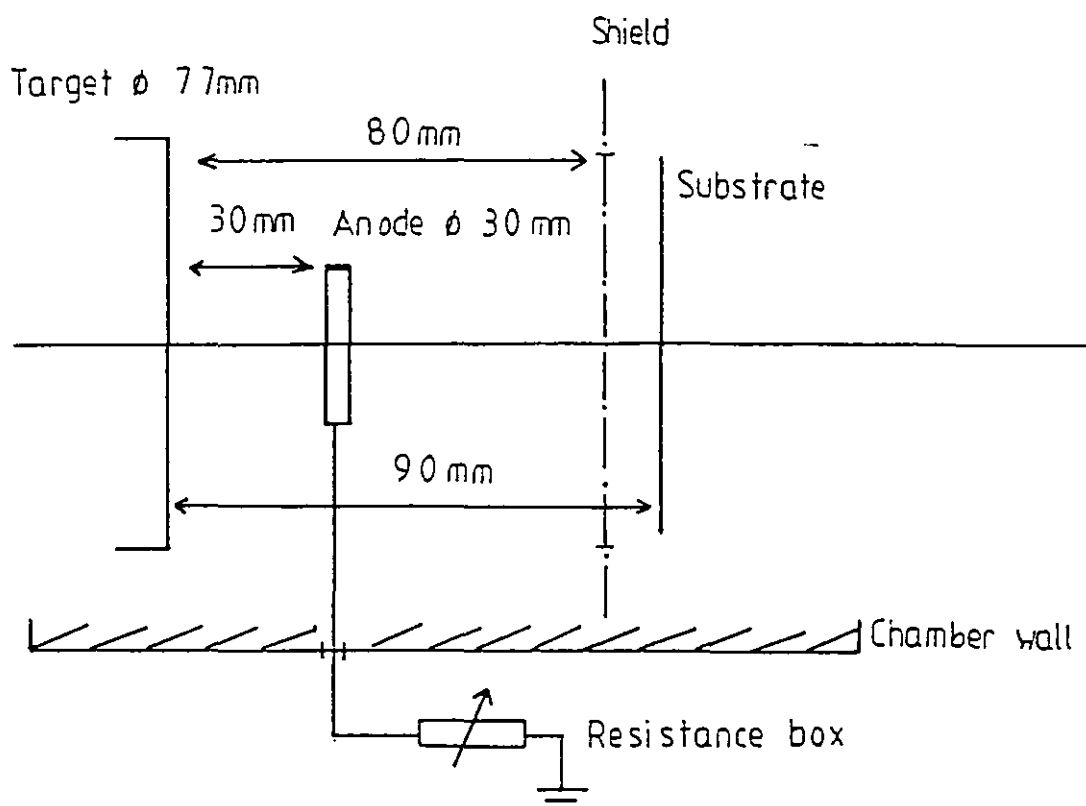


Fig.16 Schematic of Experimental Configuration.

the shield window was used to clean the substrates by means of a glow discharge. Aluminium oxidizes easily, the oxide having a low sputter yield. hence its use in the chamber since any contamination/impurities from it should be small.

The substrates are mounted on a stainless steel plate 255 mm by 150 mm and 3 mm thick. The plate is attached to a rod that passes through a vacuum collar in the chamber wall. The substrates are positioned on the backing plate such that the apparatus can be moved into a known position behind the shield window by using spacer collars as markers on the rod arm outside the chamber. The substrates are attached to the backing plate by use of insulated spring clips. A resistance thermometer was cemented to the backing plate in order to monitor the temperature variation during deposition.

Charged particles escape from the confinement trap by volume recombination in a space or surface recombination on a wall by diffusion. The effective process depends on the electron mean free path  $\lambda_e$ . If  $\lambda_e$  is not much larger than the chamber radius then the former case applies, known as Schottky theory. This is used to describe the plasma parameters in the prevailing experimental conditions (2).

The leakage of charged particles from the magnetron resulted in the anode achieving a fixed potential, measured by a voltmeter to be -25 V. Fig.18. illustrates the method employed to control the self-bias voltage at the substrate in terms of the self-bias voltage at the anode. A variable resistance box was connected between the anode and earth. The case for the anode earthed is termed the balanced magnetron configuration. This is so because the plasma to the substrate is electrically and magnetically undisturbed.

A self-bias voltage calibration curve was produced before and after the experimental period and no significant variation was noted.

### 3.3 PROBE MEASUREMENTS

Determination of probe characteristics are fairly straightforward, however, their interpretation is not. The various types of plasma with differing degrees of ionization and gas pressure accounts for this difficulty. The case considered here is of a low pressure (0.4 Pa), partially ionized ( $<1\%$ ) plasma.

The theoretical description of the current-voltage characteristics of an electrostatic probe depends not only on the plasma investigated but also on the geometry of the probe used. At the outset, the conditions outlined in Sect.2.4 are assumed to apply.

As previously explained, the generally accepted method of determining plasma parameters is by use of electrostatic (Langmuir) probes. In this instance, a single planar probe was used. The probe is a disc of Aluminium, 6 mm in diameter of thickness 0.35 mm. The contact wire is welded to the reverse side of the probe, and the wire shielded in a ceramic tube to insulate it from the discharge in which it is placed, Fig.19. The probe was mounted in a holder capable of traversal across the substrate position. Prior to use for measurement, the probe was cleaned by application of a large negative bias with respect to the plasma, to eliminate distortion of the probe characteristics.

Fig.19. illustrates the circuit employed to determine the current-voltage characteristics. All probe voltages were measured with respect to ground. The probe current was determined by the potential drop across a  $10\ \Omega$  high power, high precision resistor with a tolerance of  $\pm 1\%$  and a power rating of

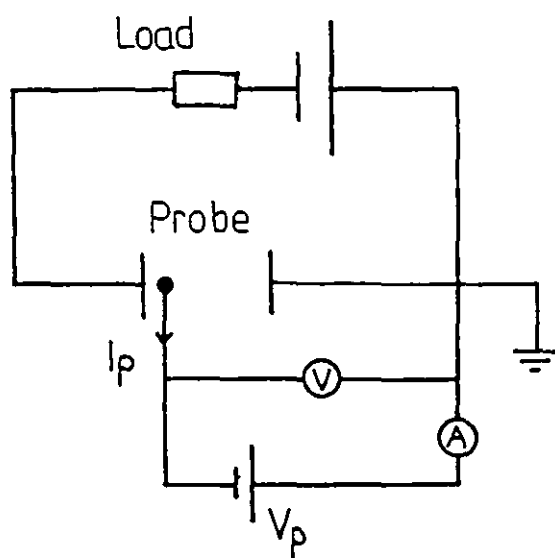
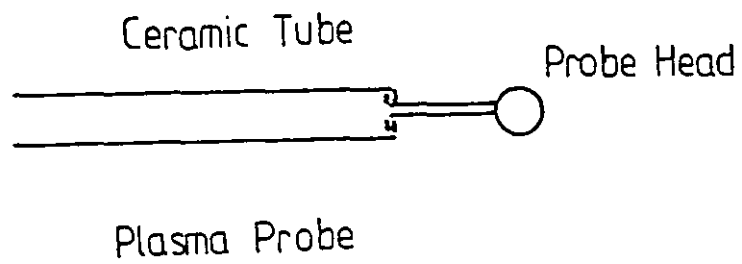


Fig.19 Single Probe Circuit.



10 W.

The potential between the probe and the grounded reference electrode can be varied so that the probe may be at either a higher or lower potential than the surrounding discharge. The current flowing from the discharge to the probe, which consists of an ion current  $I_j$  and an electron current  $I_e$ , can be determined for various values of probe voltage. This is known as a probe characteristic. For various settings of the resistance box, the self-bias voltage  $V_f$  at the substrate was noted. The self-bias voltage of the anode  $V_a$  was measured using a voltmeter. Calibration curves of  $V_a$  and  $V_f$  versus  $R$  were thus determined.

### 3.4 HEAT LOAD - EXPERIMENTAL

As a probe, an Aluminium plate 61 mm by 61 mm by 1.15 mm of mass 11.59 g was used. The probe was situated on an electrically isolated holder, the probe being thermally isolated from the holder by means of ceramic spacers. A resistance thermometer was bonded to the reverse side, using a Zinc Oxide filled Silicon compound, and used as a temperature monitor. A shield was placed in front of the probe to prevent deposition during the target sputter cleaning period.

The resistance thermometer was connected to a chart recorder via an electrical lead-through. To calibrate the temperature reading indicated by the recorder, the following procedure was adopted. Upon sealing the deposition chamber the ambient temperature was noted by reference to a mercury-in-glass thermometer. The resulting trace on the recorder enables calibration of the horizontal axis in terms of time and the vertical axis in terms of temperature. The chart recorder provided a reliable record of temperatures up to  $80^{\circ}$  C. Above this, temperatures were obtained by

connecting the resistance thermometer to a multimeter. A chart recorder traverse rate of  $5 \text{ mms}^{-1}$  proved adequate for all experiments.

### 3.5 SUBSTRATE PREPARATION

Cobalt films were deposited on two types of substrates, glass microslides 75 mm by 22 mm by 1 mm and mica slides of similar dimensions. To ensure good adhesion of the film to the glass substrates, the following cleaning procedure was adopted. The substrates were immersed in an organic solvent and placed in an ultrasonic bath for thirty minutes. The substrates were subsequently rinsed in de-ionized water and dried. Prior to deposition, the substrates were exposed to a glow discharge of 13 Pa of Argon, 7 Pa of Oxygen at 100 mA D.C., 400 V for three minutes.

Mica substrates were used to prepare samples for film examination by transmission electron microscopy (TEM). Mica slides were cleaved in half and a thin layer of Carbon ( $\approx 10 \text{ nm}$ ) deposited on the cleaved surface. This is accepted as a standard preparation technique. The advantage of this method is that the Carbon layer will separate from the mica substrate upon immersion in water. The film samples may then be mounted for TEM analysis.

### 3.6 TRANSMISSION ELECTRON MICROSCOPY (TEM)

This technique may be used to obtain information relating to the crystal size and structure of materials. However, the method places stringent limitations on sample preparation. Essentially the sample to be analyzed must be thin enough to admit passage of electrons through it. The slowing down and stopping of electrons is strongly influenced by multiple scattering processes. The practical maximum range is determined for various thicknesses of Aluminium with electrons of known energy. For an electron energy of 0.3 MeV, the range is  $78 \text{ mg cm}^{-2}$ . In practice, to obtain a

reasonable resolution, the material must be less than 200 nm thick.

Film samples were prepared as previously discussed. The samples were scored and floated off the mica substrates in a petri dish of de-ionized water.

Film material was then mounted on a 200 mesh TEM grid. The samples were studied using bright-field imaging and electron diffraction patterns.

Prominent reflections, at angles characteristic of the de Broglie wavelength of the matter waves associated with electrons and crystal plane separation, may be observed by electron diffraction from a regular lattice. This technique was originally applied to the case of X-ray diffraction and later extended.

Assuming that the crystal plane separation is  $d$ , electron wavelength  $\lambda$ , then reflection will occur at an angle  $\phi_b$  (the Bragg angle) when:

$$n \lambda = 2d \sin\phi_b$$

where  $n$  is the order of diffraction. Note,  $(n\lambda/2d) \ll 1$  is a necessary condition.

Fig.20. illustrates a typical TEM construction. The electron beam is directed toward the polycrystalline sample. The crystal orientation is random, thus for each plane separation  $d$ , some crystals will be oriented so as to produce Bragg reflection. This manifests itself as a cone of diffracted electrons incident on the plate/detector. It is possible by measuring the radii of these cones at the image plane to calculate the plane separation  $d$  for each cone. The crystal structure may be inferred upon comparison of the calculated plane separations to standards in the ASTM index.

Bright-field imaging: in this instance the electrons are passed through the sample and focused so as to produce an image. The crystals oriented for

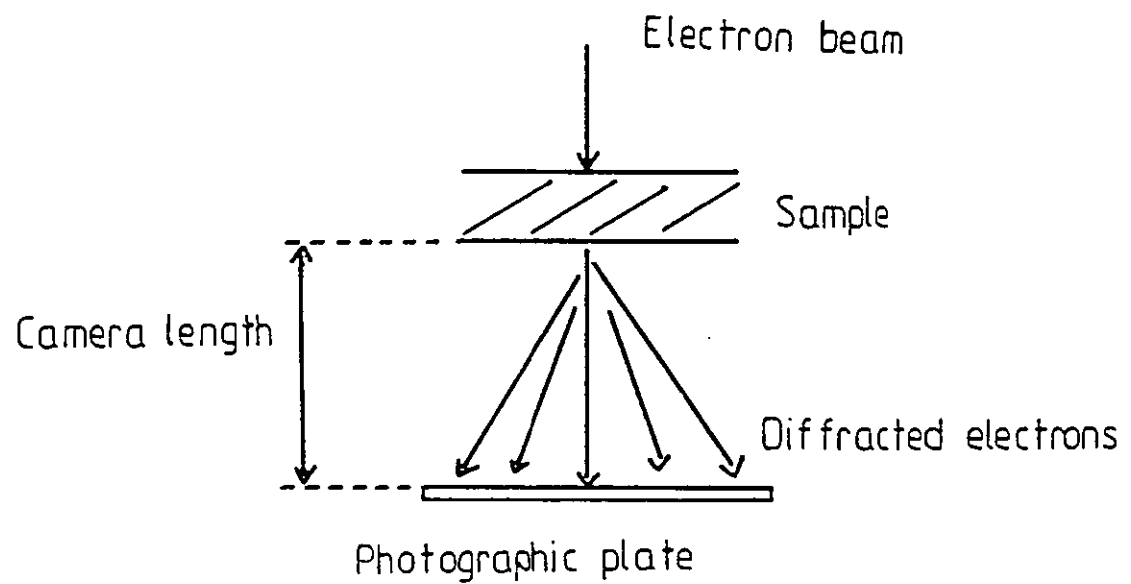


Fig.20 Schematic of electron diffraction process  
in a TEM system.

Bragg reflection diffract electrons out of the image. These are seen as dark spots on a bright background.

It is possible to obtain a rough estimate of the crystal size by this method. However, it must be borne in mind that these sizes are from crystals as projected onto an image plane. Moreover, sampling over a number of films is necessary in order to arrive at a reasonable estimate.

### 3.6 TALYSTEP SURFACE PROFILER

The device, constructed by Rank Taylor Hobson, employs a  $12.5\ \mu\text{m}$  radius diamond stylus to follow the surface contours of a material. Samples deposited on glass microslides were used. A stylus force in the range 10 to  $20\ \mu\text{N}$  for a stylus penetration of 10 nm was typical. Due to the large pressures generated, substrates with good mechanical properties are desirable. The device was manually operated, however, by careful calibration an accuracy of the order of 20 nm could be obtained.

### 3.7 ENERGY DISPERSIVE ANALYSIS BY X-RAYS (EDAX)

When a sample is subject to bombardment by energetic electrons, electrons from the inner levels of the sample may be displaced. The resulting vacancies may be occupied by electrons from higher levels. These transitions are accompanied by emission of radiation in the X-ray region of the spectrum. This X-ray spectrum is thus characteristic of the constituents of the sample. Moreover, the incoming incident electrons are subject to acceleration and deceleration by the electric fields of the sample's atoms. This results in the emission of Bremsstrahlung radiation. The sample spectrum is thus a background of Bremsstrahlung upon which the characteristic element peaks are superimposed. This process may be implemented using a combination of an electron microscope and an X-ray

analyzer. The sensitivity of the system employed here was limited to elements of atomic number greater than 11, i.e. from Sodium onwards.

### 3.9 MAGNETIC MEASUREMENTS

Fig.21. illustrates the instrument used to measure the coercivity of the deposited films. The pick-up coils are arranged to intercept a large fraction of the magnetic flux from the poles at the film edges. The magnetization in the film varies with time in response to an applied alternating field. By Faraday's law of electromagnetic induction, a voltage is induced in the pick-up coil which is proportional to the rate of change of flux linking it. The compensated pick-up voltage after integration and amplification is applied to the vertical plates of an oscilloscope. A voltage which is proportional to the excitation field is applied to the horizontal plates of the oscilloscope. The resulting trace is a hysteresis loop of the sample. After suitable calibration of the axes the sample coercivity can be determined.

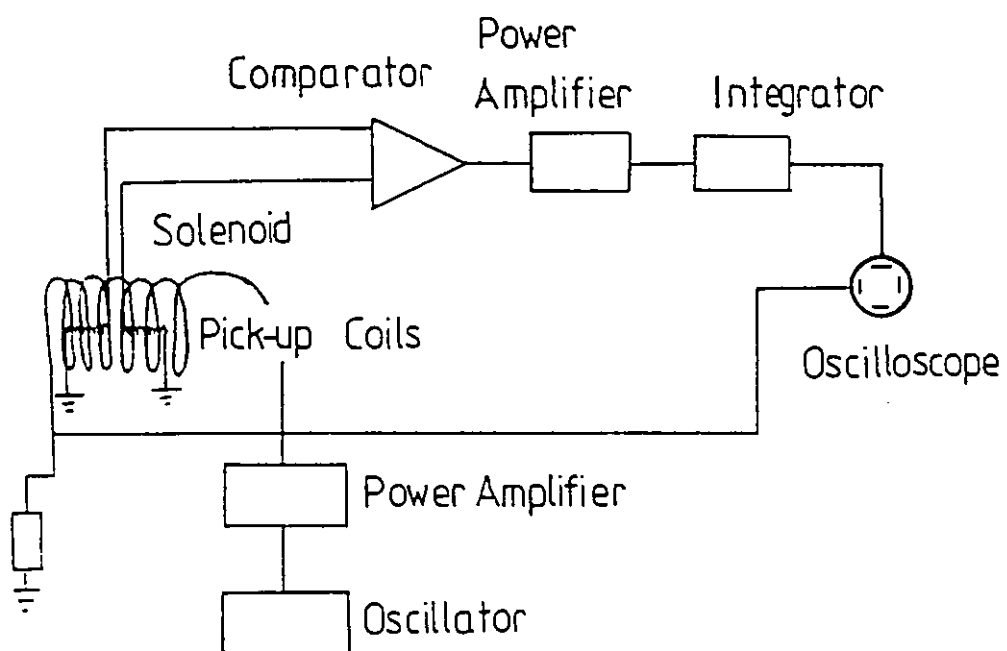


Fig.21 Hysteresisgraph-loop tracer.

### 3.REFERENCES

- 1) Maissel L. and Glang R., Handbook of Thin Film Technology, McGraw Hill, New York (1970), Chap.4.
- 2) Sin-Li Chen and Sekiguchi T., J.Appl. Phys., 36 (1965), p.2363.



4. RESULTS

4.1 SELF-BIAS VOLTAGE CALIBRATION

Fig.22. illustrates the self-bias voltage calibrations for the substrate and anode as a function of the resistance box setting. The error bars on the voltage are  $\pm 0.5$  V. The calibration was performed before and after the experimental period. The conditions pertaining to these calibrations were:

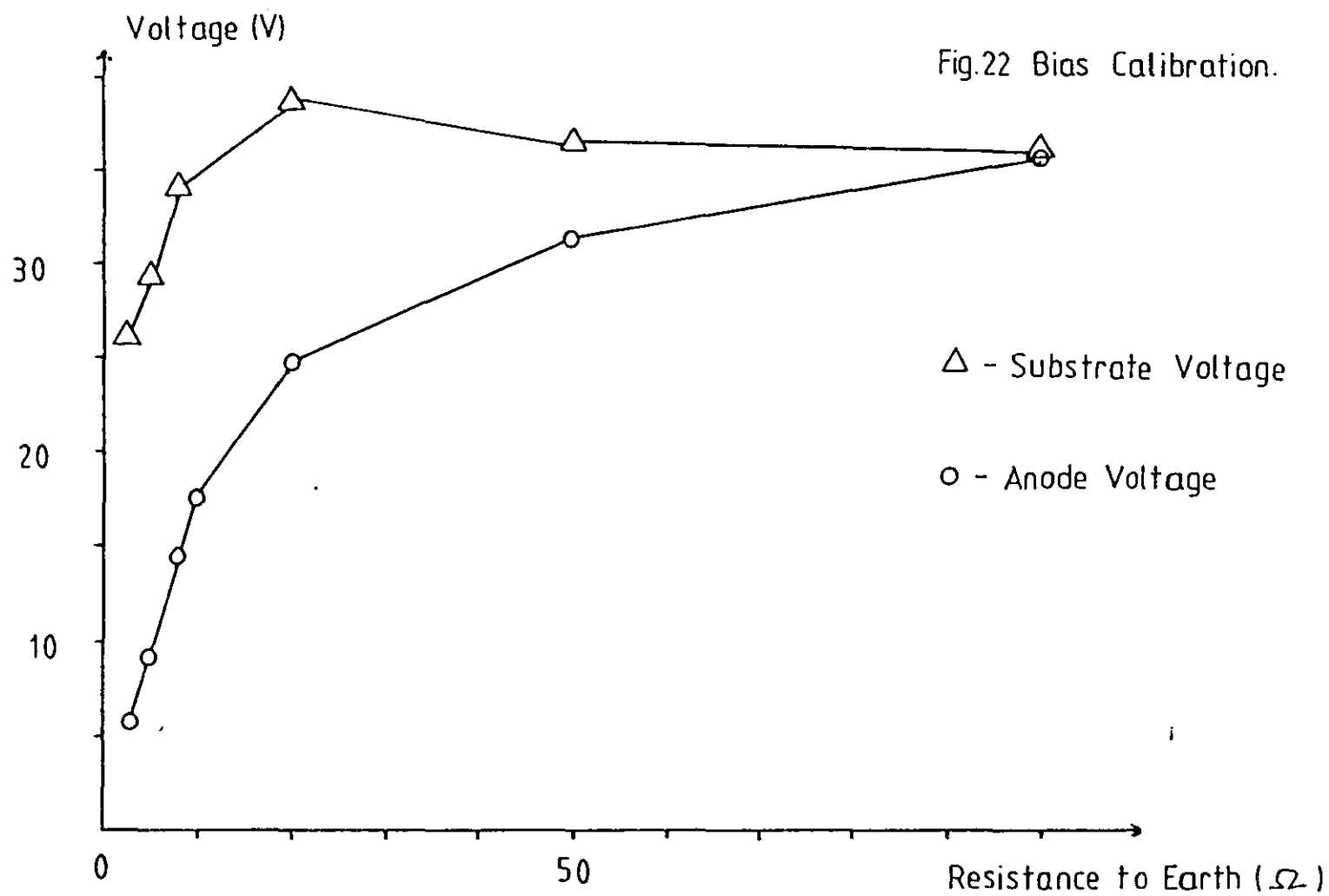
Chamber Base Pressure	$3 \cdot 10^{-3}$ Pa
Argon Gas Pressure	0.4 Pa
Target to Anode distance	30 mm
Target to Substrate distance	90 mm
Magnetron Power	0.9 Kw

4.2 HEAT LOAD

Table 1.

Applied Power Density ( $\text{Wcm}^{-2}$ )	Resistance Setting ( $\Omega$ )	Rate of Temperature Rise ( $\text{Ks}^{-1}$ )	Power at Probe ( $\text{Wcm}^{-2}$ )	Percentage of Applied Power Developed at Probe
18.59	Floating	0.56	0.16	0.86
18.25	20	0.36	0.10	0.55
18.17	3	0.27	0.08	0.44

The above table was prepared from data obtained by measuring the rate of temperature rise of a probe as discussed in Sect.2.5. The experimental conditions were similar to those previously outlined, Fig.23. Illustrates



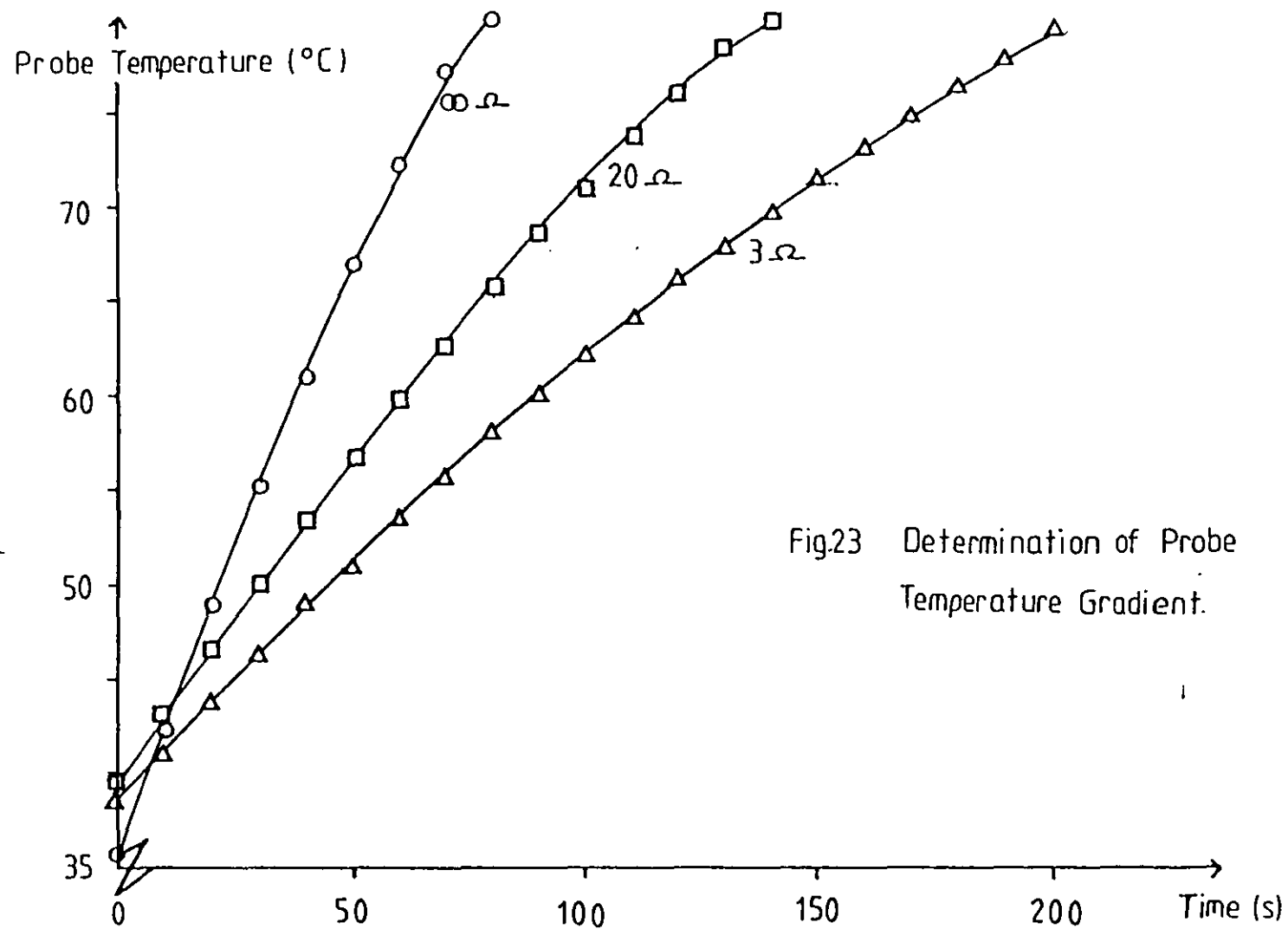


Fig.23 Determination of Probe Temperature Gradient.

the initial rate of temperature rise of the probe under the given conditions.

### 4.3 PLASMA PROBE MEASUREMENTS

To determine the electron temperature  $T_e$ , the positive ion current is extrapolated and subtracted from the total probe current.  $T_e$  is found by plotting the net probe current versus probe voltage, the slope of the plot is  $q/kT_e$ .

The conditions outlined in Sect.2.4 approximate to the ideal. For the real case of a low pressure glow discharge, the electric field can produce relatively large numbers of energetic electrons or even produce a bimodal distribution (1). The electron distribution is unlikely to be Maxwellian. The concept of electron temperature is thus not strictly valid, however, it is generally used and is taken to be the slope in the electron retarding region of the characteristic.

The choice of probe is normally dictated by the type of plasma to be investigated. It is more usual to use double probes or cylindrical probes for the type of sputtering discharge used here (2). It has been found that results obtained by the use of single probes are within a factor of two of the above methods (2).

Table 2.

Resistance Setting ( $\Omega$ )	Ion Saturation Current(mA)	Electron Temperature (eV)	Current to Probe at +1V (mA)	Species Sheath Density $n_{is} \text{ (m}^{-3}\text{)}$	Debye Length ( $\mu\text{m}$ )
infinite	5.45	$3.1 \pm 0.2$	320	$4.4 \cdot 10^{17}$	15
20	2.24	$6.96 \pm 0.35$	144	$1.3 \cdot 10^{17}$	42
8	1.57	$6.18 \pm 0.31$	98	$9.0 \cdot 10^{16}$	48
3	1.48	$6.13 \pm 0.31$	84	$8.5 \cdot 10^{16}$	49

The above table was prepared from data obtained from probe techniques outlined in Sect.3.3. Probe characteristics were plotted for the ion current saturation region and electron retarding region and are illustrated in Fig.24.

#### 4.4 DIFFRACTION PATTERNS and BRIGHT-FIELD IMAGES

Figs. 25a, 25b, 25c illustrate the diffraction patterns obtained for films deposited under various conditions. The resolution is poor, limiting visual clarity as will be discussed later. However, the patterns appear to indicate that the films are polycrystalline.

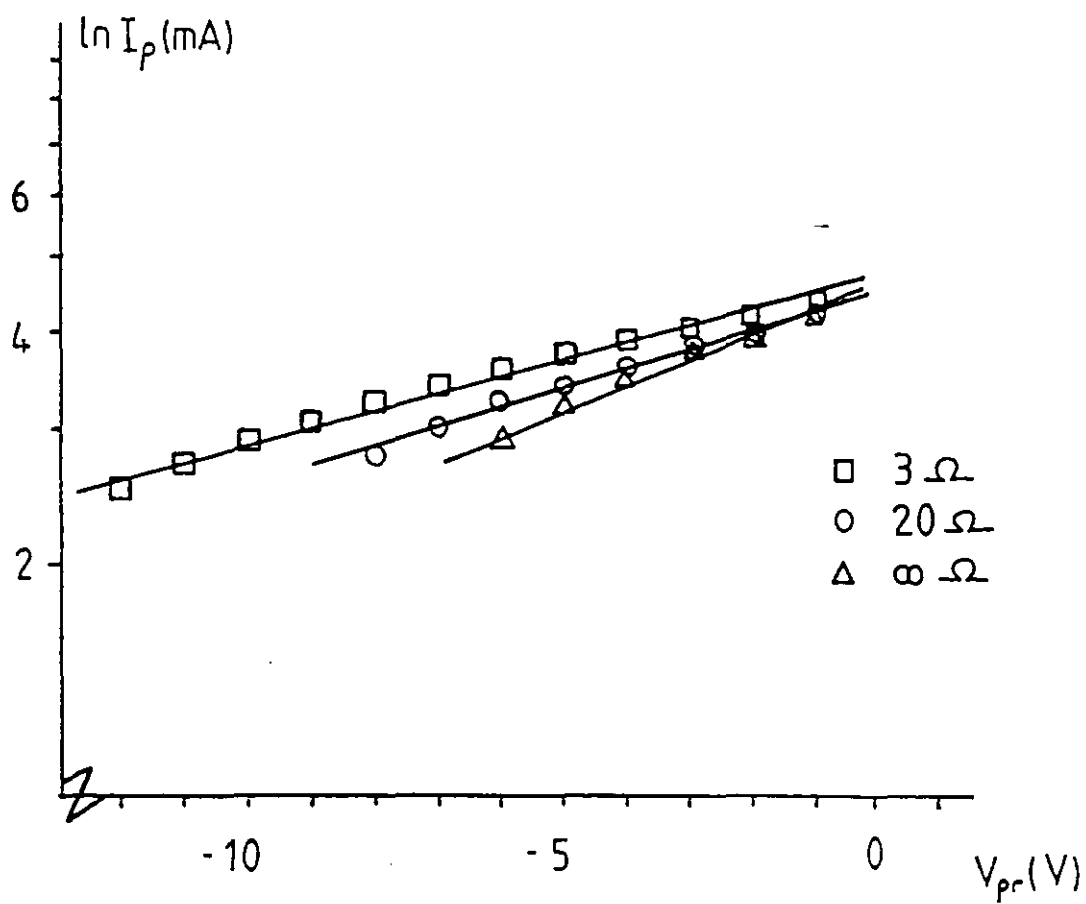


Fig.24 Plasma probe characteristic.

7625603



Fig 25a Diffraction pattern for  
film of balanced magnetron

7625606



Fig 25 b Diffraction pattern for  
film of self bias -25V



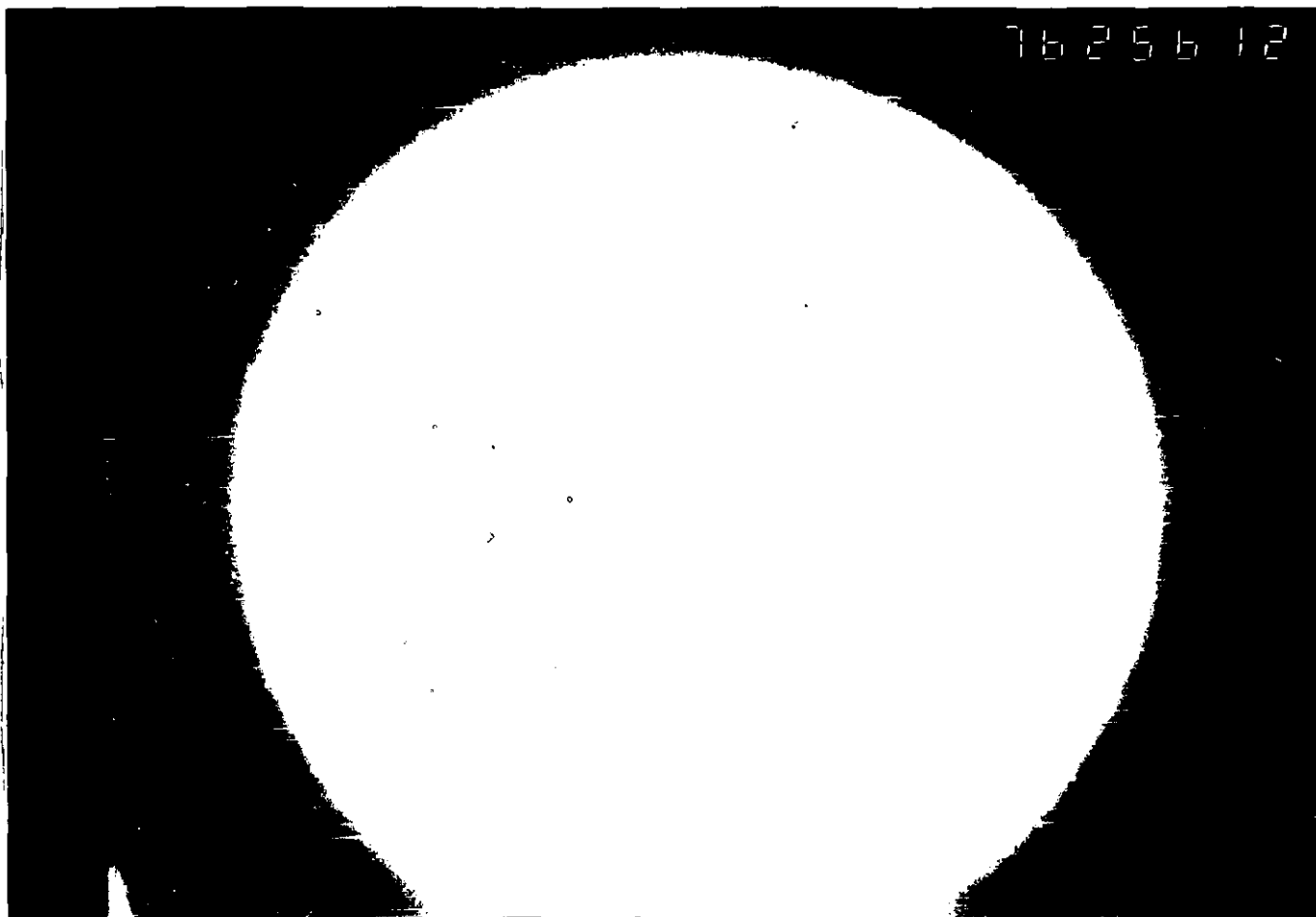
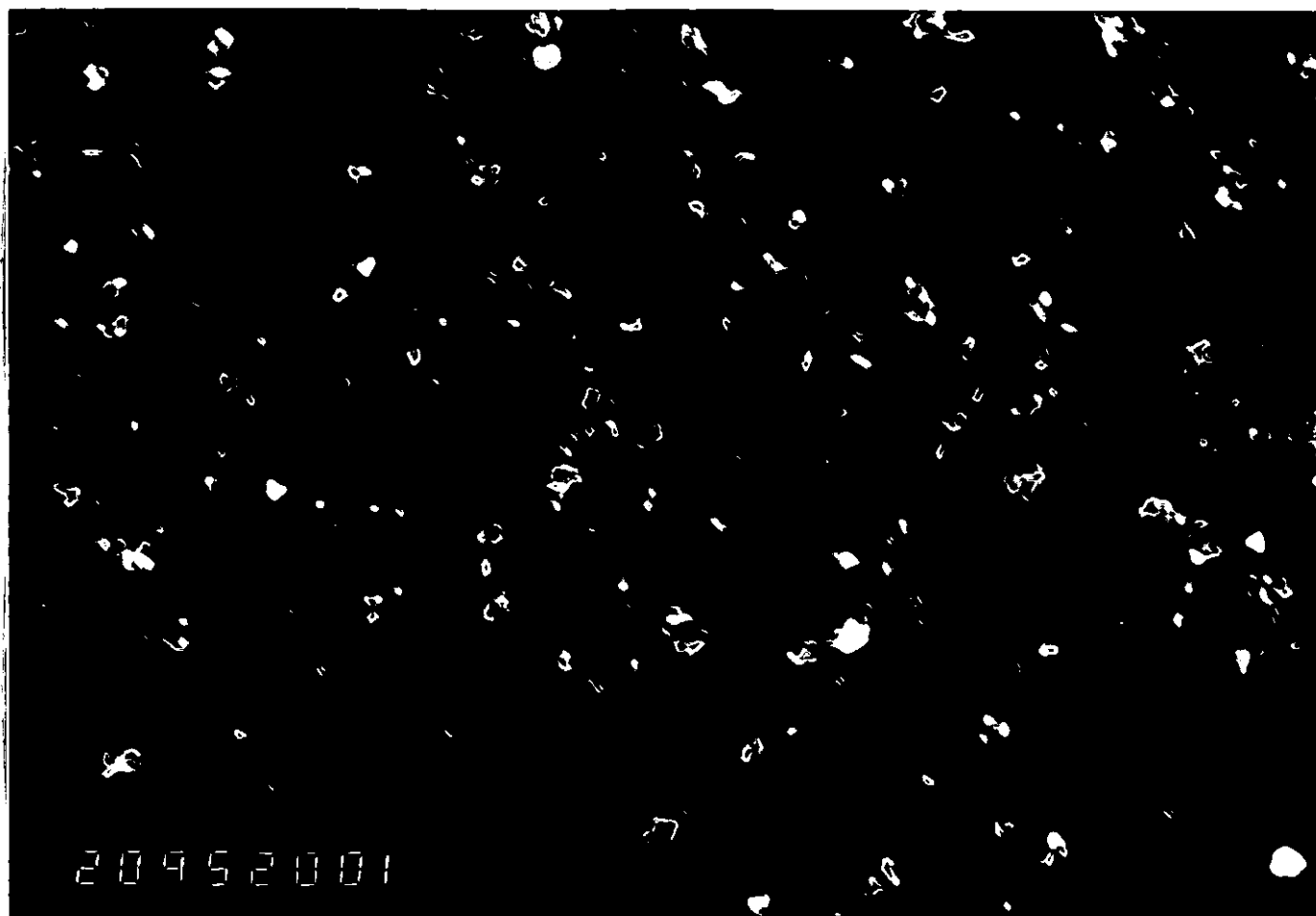


Fig 25c Diffraction pattern for  
film of self bias -39V

Table 3.

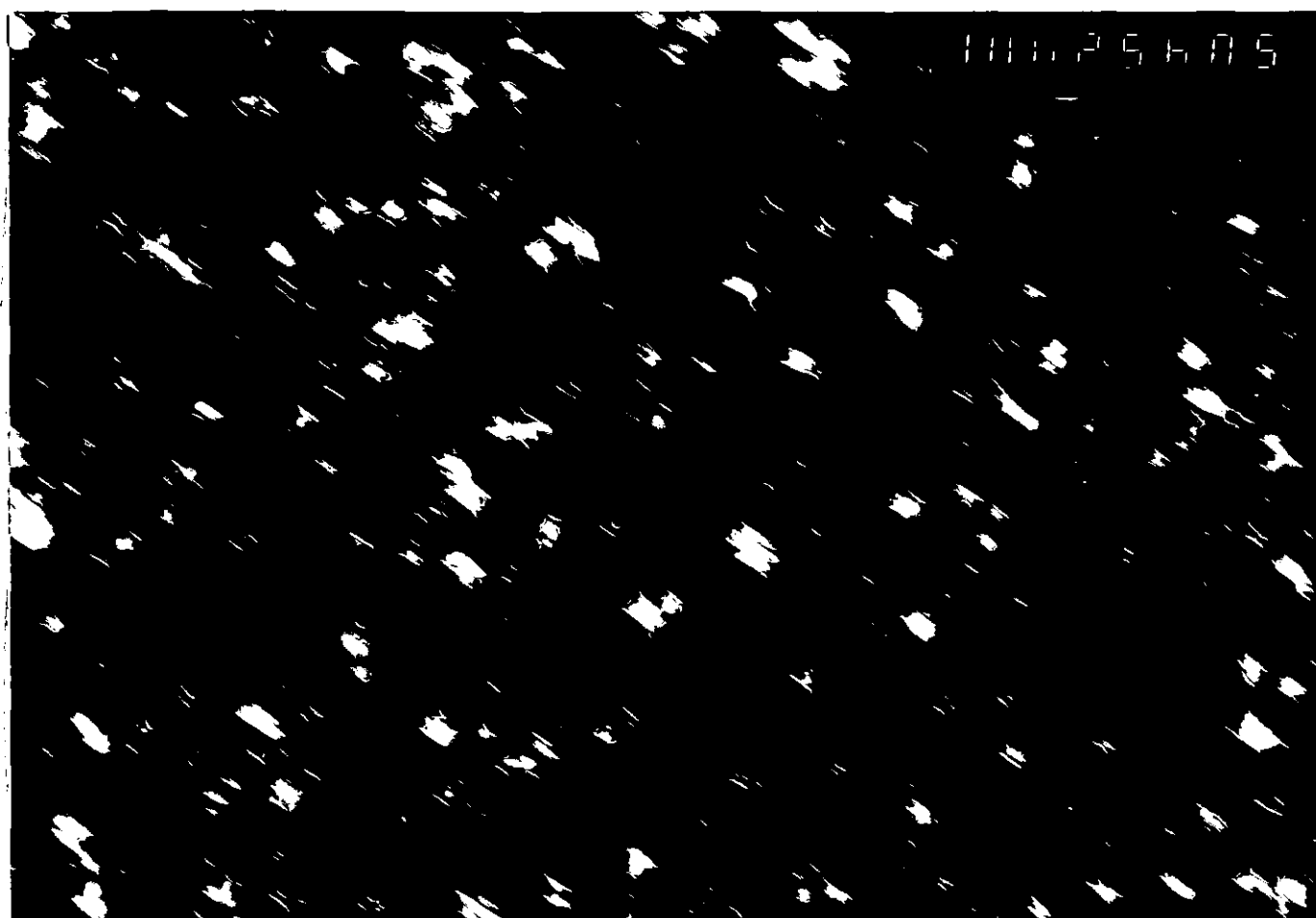
Bias (V)	Ring No.	Diameter (mm $\pm 0.25$ )	Plane Separation $d$ ( $10^{-10}$ m)	Standard ASTM Index ( $10^{-10}$ m)	Phase	h, k, l
-25	1	27.25	$2.06 \pm 0.3$	2.0467	FCC	1, 1, 1
	2	28.0	$2.01 \pm 0.3$	2.023	HCP	0, 0, 2
	3	29.0	$1.94 \pm 0.3$	1.910	HCP	1, 0, 1
	4	31.25	$1.80 \pm 0.3$	1.7723	FCC	2, 0, 0
	5	40.5	$1.39 \pm 0.2$			
	6	54.0	$1.04 \pm 0.2$	1.047	HCP	2, 0, 1
	7	55.0	$1.02 \pm 0.2$	1.0233	FCC	2, 2, 2
-39	1	27.25	$2.06 \pm 0.3$	2.0467	FCC	1, 1, 1
	2	28.0	$2.01 \pm 0.3$	2.023	HCP	0, 0, 2
	3	29.0	$1.94 \pm 0.3$	1.910	HCP	1, 0, 1
	4	31.25	$1.80 \pm 0.3$	1.7723	FCC	2, 0, 0
	5	40.5	$1.39 \pm 0.2$			
	6	53.5	$1.05 \pm 0.2$	1.047	HCP	2, 0, 1
	7	54.75	$1.03 \pm 0.2$	1.0233	FCC	2, 2, 2

Figs. 26a, 26b, 26c illustrate the corresponding bright-field images. It is noted that the crystal size is in the range 10 to 50 nm. From X-ray diffraction techniques and magnetic measurements it is difficult to draw any firm conclusions about the films. Due to the apparently small crystal size and high packing density, the films could conceivably consist of Cobalt grains embedded in an amorphous Cobalt background, or in a background of superparamagnetic particles. The crystal size distributions are shown in



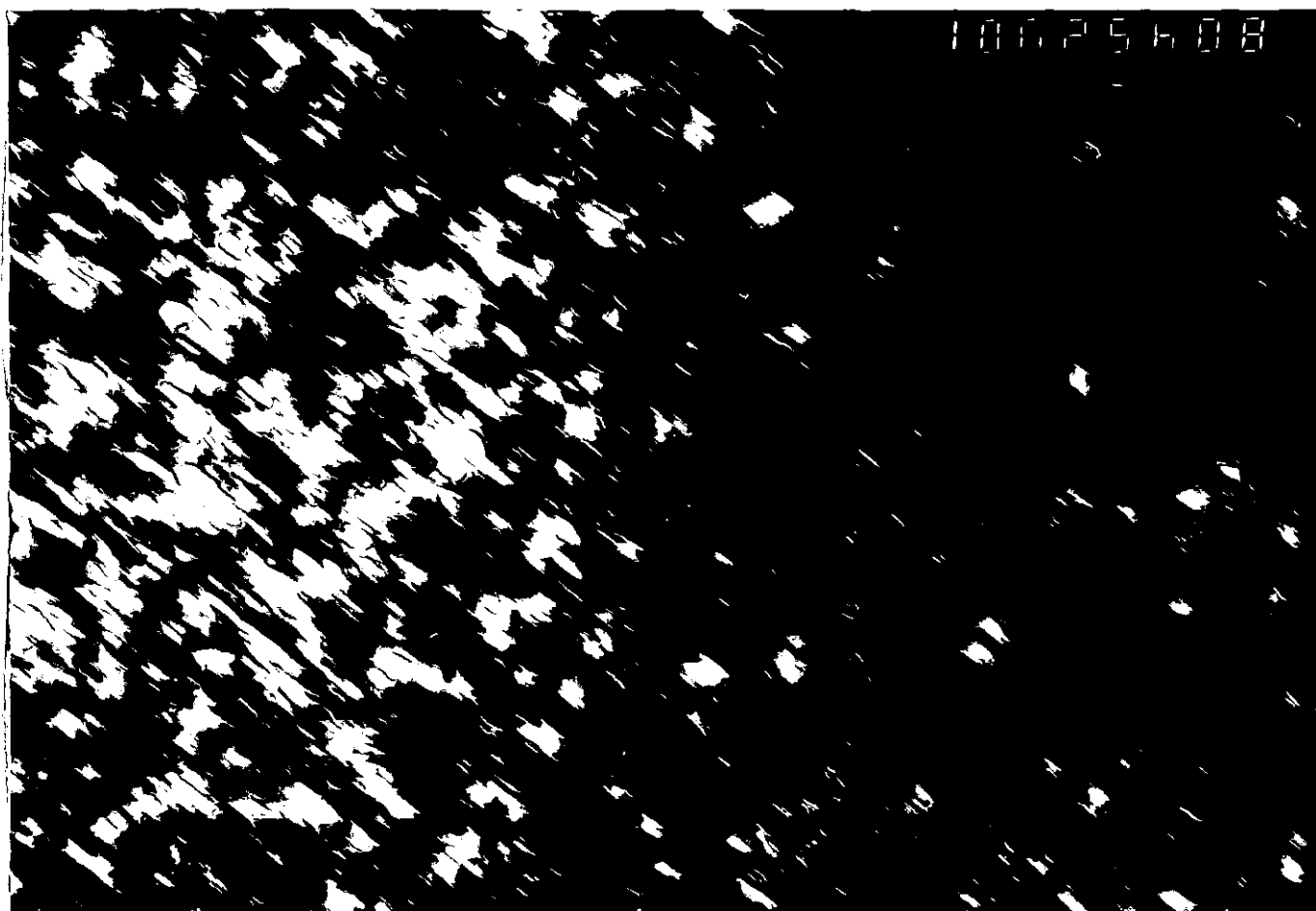
50 nm

Fig 26a Bright field image for fig25a



50 nm

Fig 26 b Bright field image for fig 25 b



50 nm

Fig 26c Bright field image for fig 25c

Figs.27.

Fig.28 illustrates a cross-sectional view of a film deposited with the anode earthed. The film exhibits a columnar-voided type structure typical of low  $T/T_m$  in accordance with the zone model of Movchan and Demischin.

#### 4.5 EDAX

The film composition was analyzed by EDAX, the elements looked for being Cobalt, Iron and Aluminium. Figs. 29a, 29b illustrate the composition of films deposited at biases of -25 V and -39 V, and table 3 lists the film compositions.

Table 3.

Bias (V)	Percentage Composition		
	Co	Fe	Al
-25	91.979	7.447	0.574
-39	92.001	7.746	0.253

The Iron content is due to sputtering of the magnetron pole pieces. The presence of a small amount of Aluminium could be expected due to the fittings used in the chamber. The film composition is seen to vary, with a slight increase in Cobalt and Iron content for increasing bias. This may possibly be accounted for by target aging altering the deposition erosion profile of the target. The Silicon and Calcium peaks in the figures originate from the glass microslides used as film substrates.

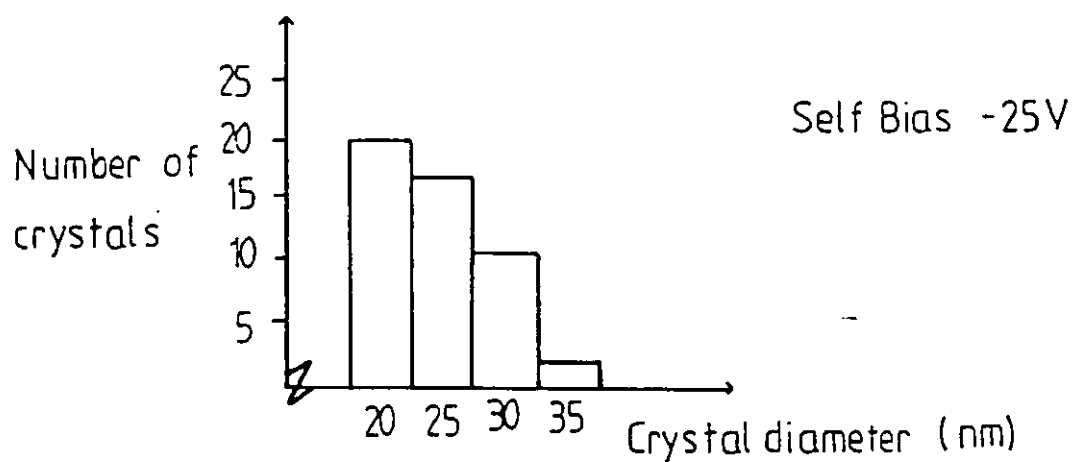


Fig27 Crystal Size Distributions.

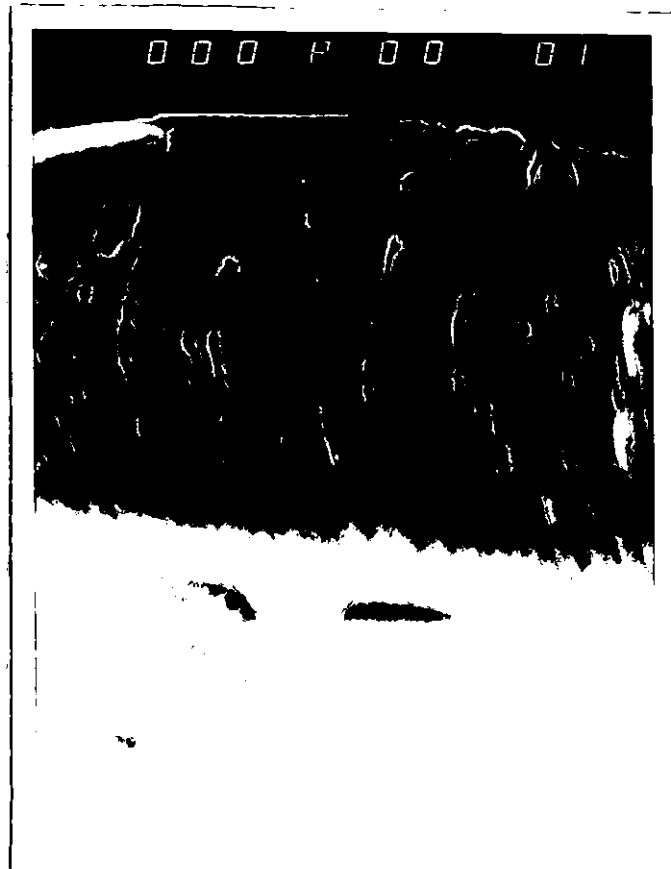


Fig28 TEM cross section for film  
deposited with anode earthed



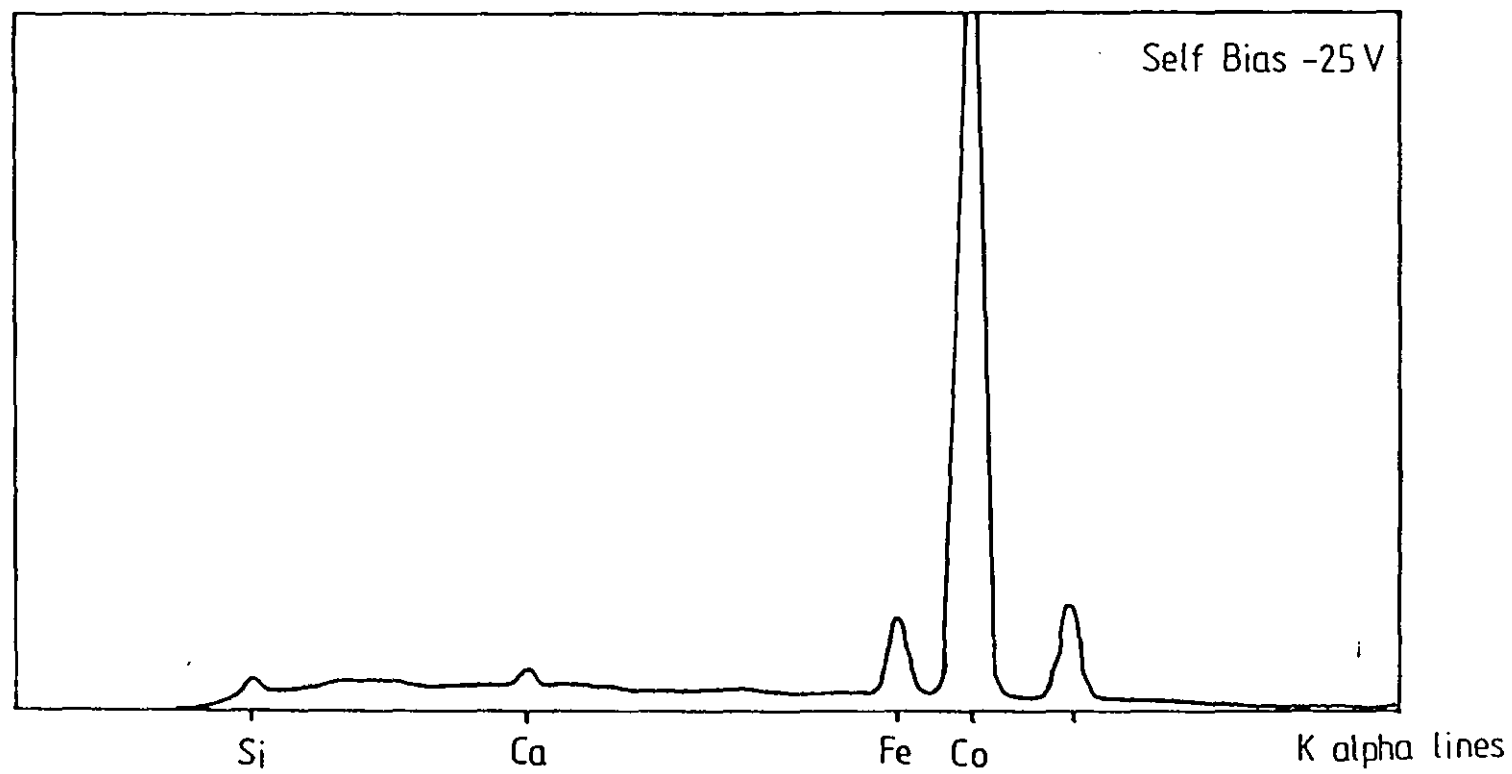


Fig29a Edax Analysis

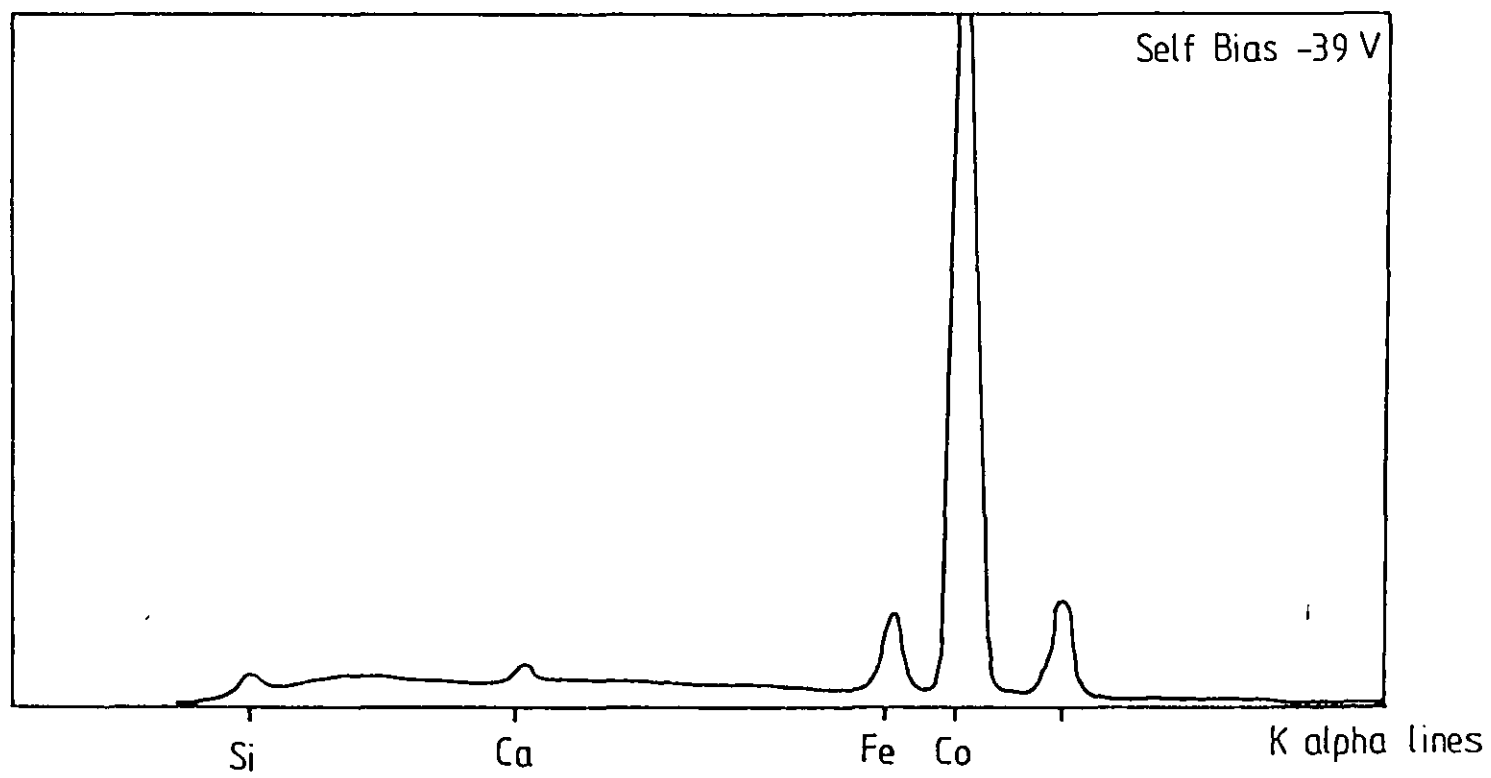


Fig29b Edax Analysis

#### 4.6 MAGNETIC MEASUREMENTS

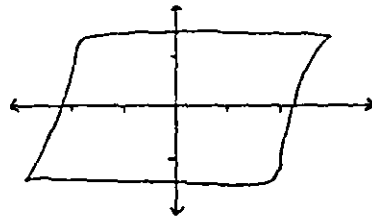
Table 4.

Resistance ( $\Omega$ )	Bias (V) $\pm 0.5$	Coercivity ( $\text{kAm}^{-1}$ )
0	Earth	2.3 $\pm 0.2$
3	-25	3.5 $\pm 0.3$
8	-34	2.8 $\pm 0.3$
20	-39	2.0 $\pm 0.1$
Infinity	-36	1.8 $\pm 0.1$

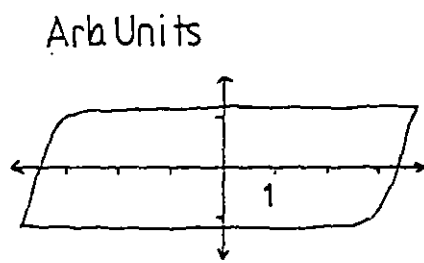
The above table was prepared from data extracted from the hysteresis loops illustrated in Figs. 30a, 30b, 30c, 30d. The horizontal loop axis is calibrated in  $\text{kAm}^{-1}$  to give direct values of magnetic field H. The vertical loop axis is calibrated in arbitrary units. The observed trend of a maximum in coercivity with increase in bias was reproducible over the films deposited. The above data is based on three sets of films.

#### 4.7 MAGNETIC FIELD CONFIGURATION

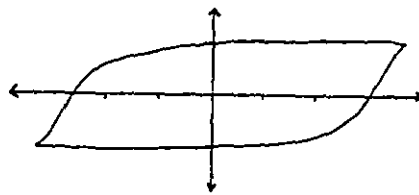
Fig.31 illustrates the magnetic field configuration of the magnetron employed in the deposition process. The lower figure is an Iron filing profile of the field along the axis of the magnetron. The upper figure is a portion of a contour map for the same configuration. It is seen that both the anode and the substrate locations are in regions of constant field. The field along the axis decreases with distance from the target.



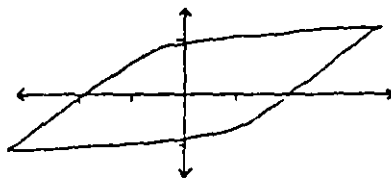
a) (Earthed Anode)



b) Self Bias -25 V



c) Self Bias -34 V



d) Self Bias -39 V

Fig 30 Hysteresis Loops under various Bias conditions

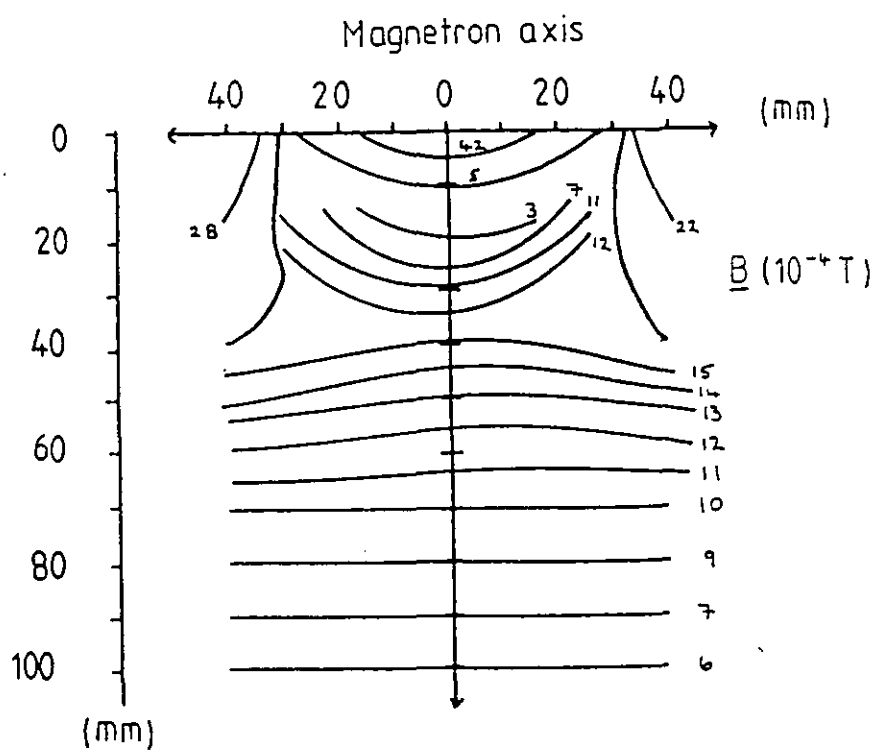
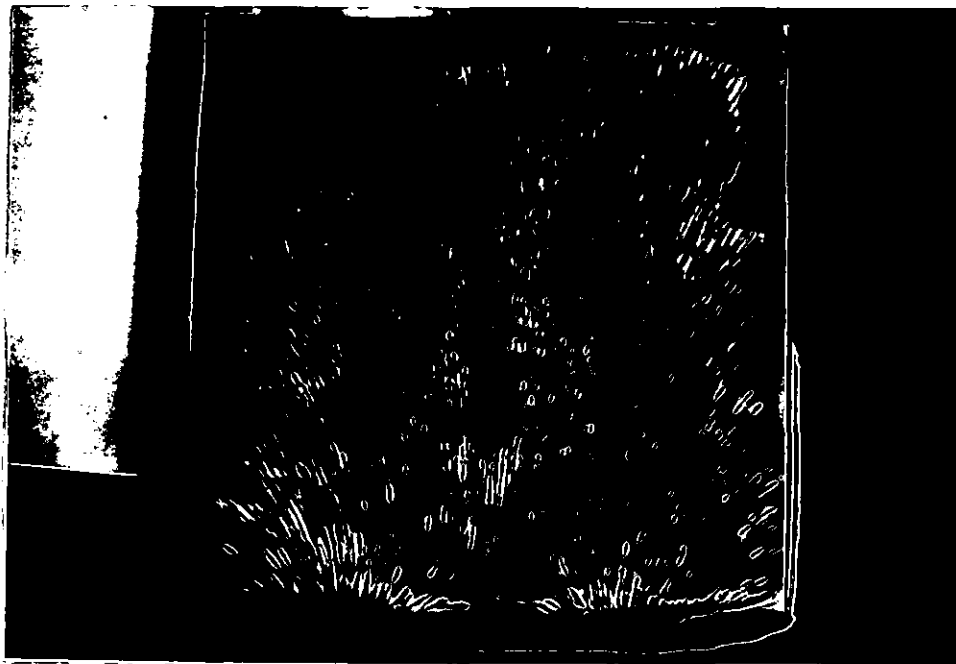


Fig31 Magnetic field configuration.

#### 4.8 PLASMA BEAM CONFIGURATION with SELF-BIAS

Fig.22 of Sect.4.1 illustrates the self-bias voltage as a function of resistance to earth. The following photographs, Figs. 32a, 32b, 32c, 32d, illustrate the plasma beam in the chamber corresponding to various values of resistance.

For the case of a balanced magnetron, the beam appears to be confined to the anode region. Upon increasing the self-bias the plasma is seen to leak away from this region and impinge on the substrate. Note, the increase of radiation intensity with increasing self-bias together with the change in beam configuration. Moreover, for a resistance to earth greater than  $20\ \Omega$ , the eye is unable to discern any change in beam intensity.

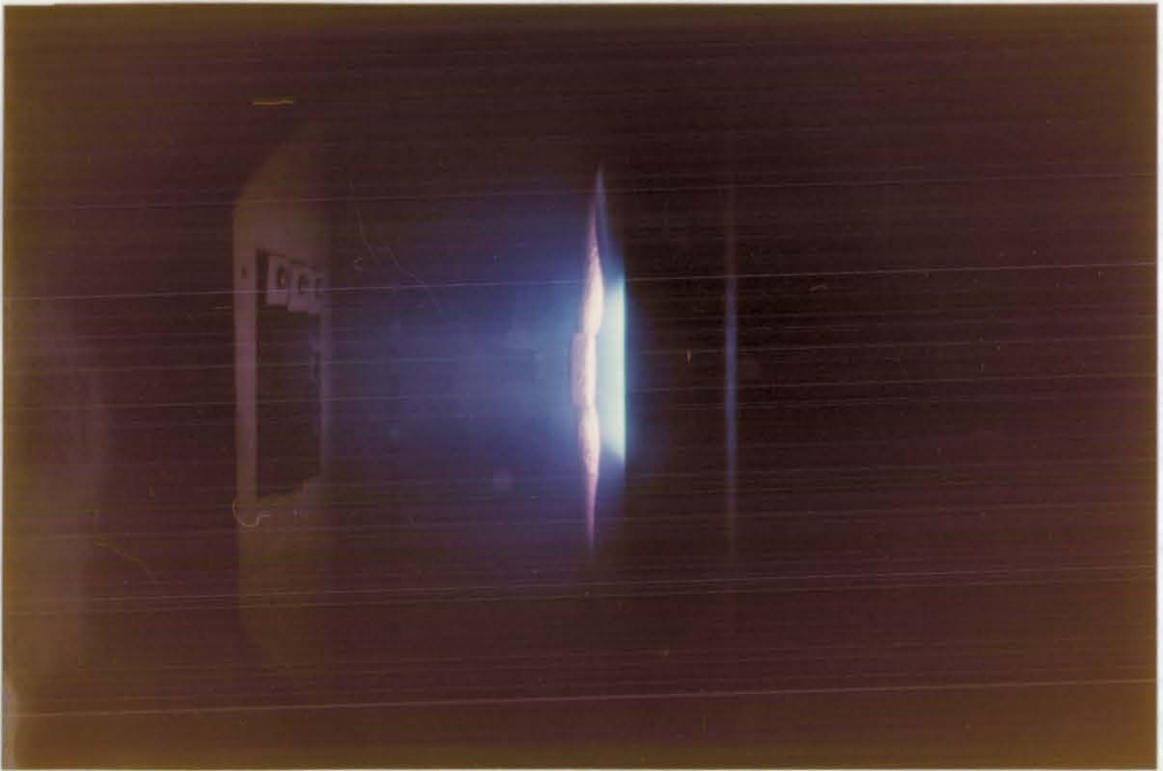


Fig 32a Chamber plasma beam  
with anode earthed

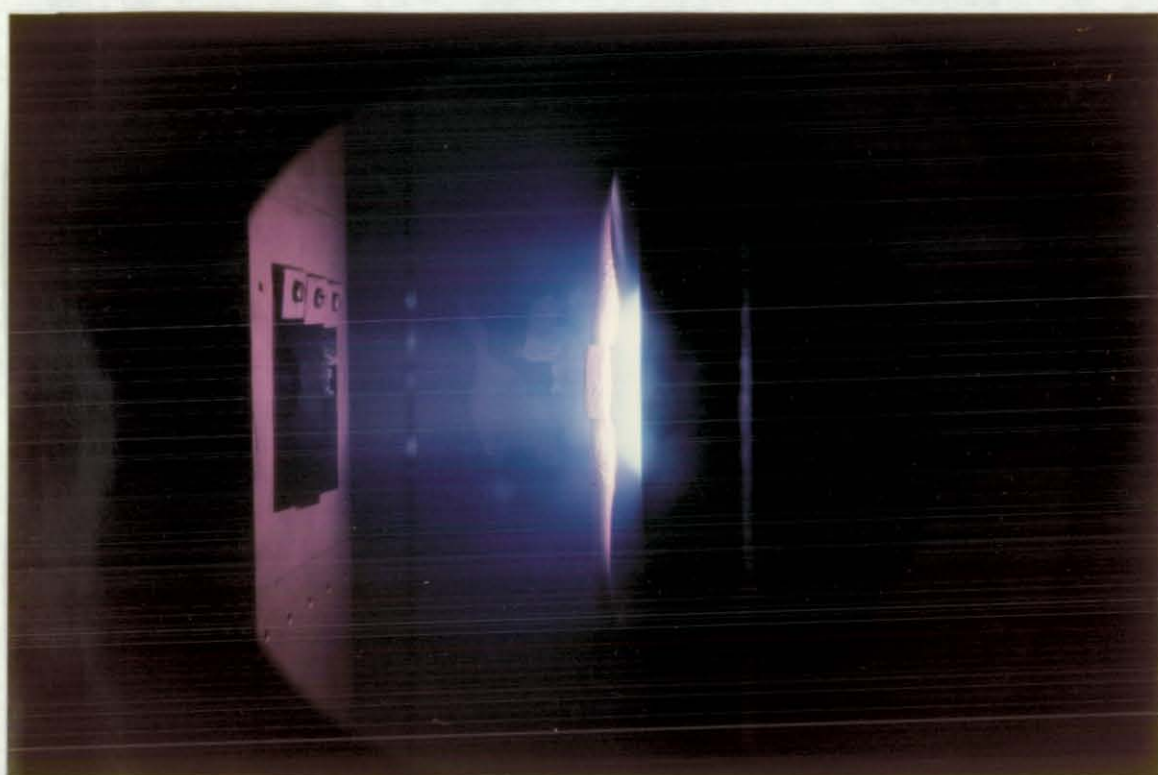


Fig 32b For self-bias of  $-25\text{V}$



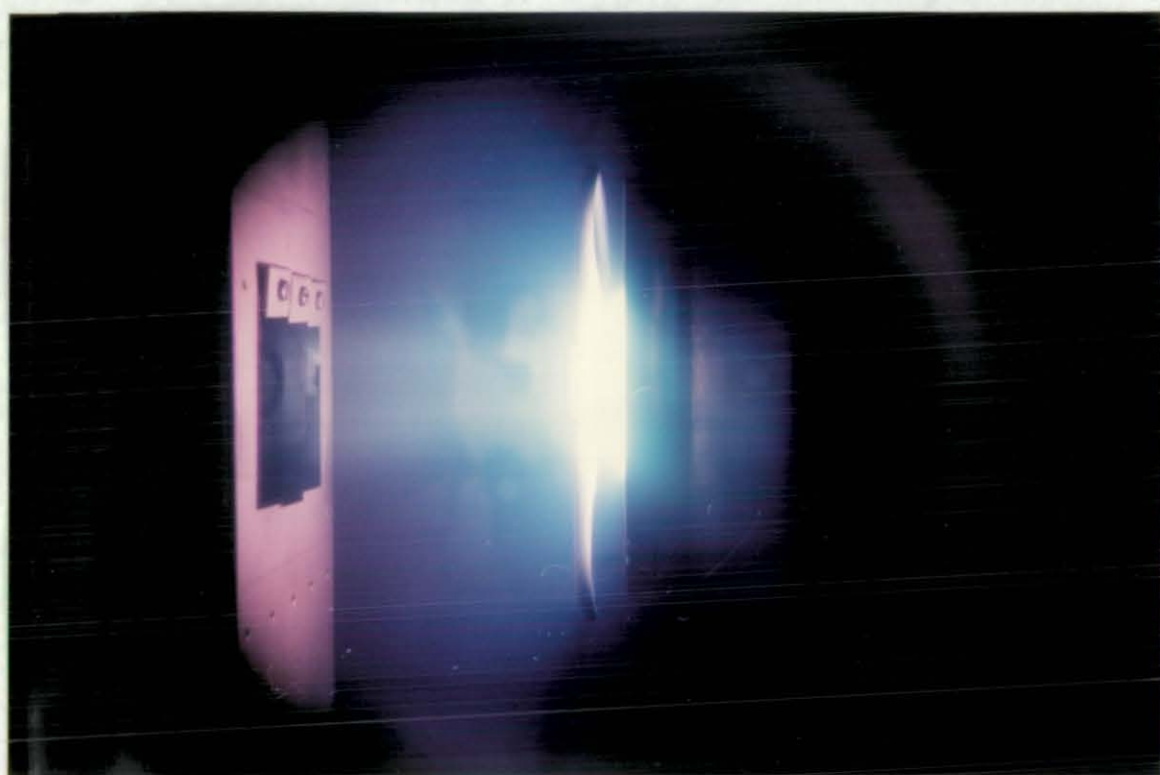


Fig32c For self-bias of  $-34\text{V}$

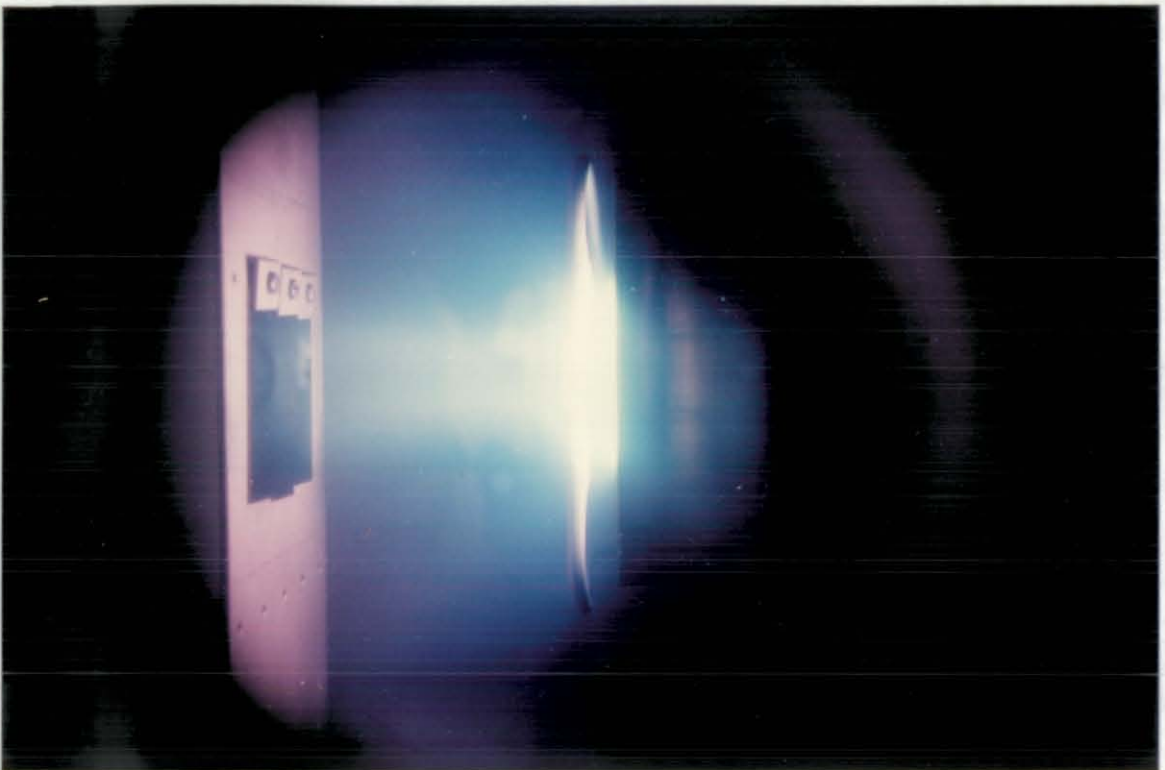


Fig32d For self-bias of  $-39V$

#### 4. REFERENCES

- 1) Thornton J.A, J.Vac. Sci. Technol., 15 (1978), p.188.
- 2) Ball D.J., J.Appl. Phys., 43 (1972), p.3047.

## 5. DISCUSSION of RESULTS

### DEPOSITION PARAMETERS

Base Pressure	$3 \times 10^{-3}$ Pa
Deposition Pressure	0.4 Pa
Magnetron Current	2 A
Magnetron Potential	-500 V
Target to Substrate Distance	90 mm
Deposition Rate	$1.5 \text{ nm s}^{-1}$

The target was a circular disc of Cobalt, diameter 77 mm and 1 mm thick. Films were deposited for about six minutes. Talystep measurements gave a deposited film thickness of  $550 \pm 10$  nm.

#### 5.1 FILM COMPOSITION

The EDAX analysis of a range of films is given in Sect.4.5. The results confirm that sputtering of Aluminium is low, hence its suitability as a shield material in the chamber. The Iron content could not be controlled though it was assumed to originate from sputtering of the magnetron pole pieces. The film composition could only be determined for elements after Sodium in the periodic table, a limitation of EDAX. The Oxygen content, if any, of the film was thus not determinable. With the given limitations, the percentage content of Iron and Cobalt were seen to increase slightly with increasing bias. The effective increase in Iron content may not be expected to significantly affect the film properties, as the Cobalt concentration is expected to dominate the magnetic properties of the films. In this instance, the effect of self-bias on the film composition is not expected to influence the film magnetic properties to any great extent.

## 5.2 SUBSTRATE HEAT LOAD

The fraction of applied power developed at the substrate position was estimated by measuring the initial rate of temperature rise of a probe, as previously explained in Sect.3.4. The initial rate of rise is used, as opposed to equilibrium temperatures, in order to avoid the problems associated with energy exchange by thermal radiation. In view of the proposed assumptions, the time for the probe to attain an equal temperature distribution should be known. It was not possible to perform transient measurements, so the following was adopted to provide an estimate. Consider the Fourier series analysis of the heat conduction equation, in one dimension, for the simple case of a plate bounded by planes  $x = 0$ ,  $x = a$ , whose surfaces are kept at constant temperature. The time dependent term is of the form  $\exp[-(n\pi K_t/a)^2 t]$ , where  $K_t^2$  is the thermal diffusivity ( $k_t/\rho c_p$ ) and  $n$  is an odd integer. This gives the time for the passage of heat through the plate as approximately 1.5 ms. This is considerably less than the response time of the chart recorder. The assumptions and approximations used to determine the absorbed power density at the substrate would appear to be quite reasonable.

The experimental data is summarized in Sect.4.2 and Fig.23. The figure illustrates the measured initial rate of temperature rise under various conditions. Ideally, the measurements should commence from the same initial conditions. However, this was impossible to ensure in practice and is reflected in the slight variation of initial temperature of the probe.

The most notable feature from the table is the relatively small fraction of applied power developed at the target. As previously given, it is usual in magnetron sputtering systems to see at least 70% of the applied power dissipated at the magnetron as heat. Of the remaining fraction, 25% or so is dissipated at the anode as heat (that is why it is water cooled). The experimentally determined ratio of absorbed to incident power densities are in reasonable agreement with similar experiments on Titanium Dioxide ( $\text{TiO}_2$ ), (1).

The deposition rate for Cobalt decreased slightly as bias increased. For a self-bias of -25 V a rate of  $5.4 \cdot 10^{-6} \text{ kgm}^{-2}\text{W}^{-1}\text{s}^{-1}$  was found, as opposed to a rate of  $5.04 \cdot 10^{-6} \text{ kgm}^{-2}\text{W}^{-1}\text{s}^{-1}$  for a bias of -39 V. This corresponds to metal atom fluxes, to the plasma probe, of  $1.4 \cdot 10^{18} \text{ s}^{-1}$  and  $1.3 \cdot 10^{18} \text{ s}^{-1}$  respectively. The ion currents for these biases yield particle fluxes of  $9 \cdot 10^{15} \text{ s}^{-1}$  and  $1.5 \cdot 10^{16} \text{ s}^{-1}$  respectively. The apparent difference in the flux magnitudes, between metal atoms and ions, is due to the fact that in a magnetron system the plasma is mainly confined to the anode target-area. The effect of the magnetic field configuration is an additional factor in determining the fluxes (2). The data obtained is in reasonable agreement with that of Window and Savvides (2) for the type of magnetron configuration employed.

The prevailing plasma condition of a low Argon pressure implies that sputtered atom transport to the substrate is virtually collisionless. Their average energy is around 10 eV as already given. Incident ion energy at the substrate is approximately  $qV_f$ . The measured substrate temperature is less than that expected of the deposited species and may be accounted for in terms of energy distribution at the substrate. It is known that a single ion can initiate up to thirty interactions at a substrate (3). Water

cooling of the target is sufficient to reduce the thermal radiation to the substrate to a negligible amount (4). The substrate heat load, for a magnetron system, can be explained in terms of sputtered atom kinetic energy, plasma radiation, heat of condensation and ion neutralization. The effects of plasma radiation are assumed small as gas temperature is not much above ambient. From the available data, table 2. Sect.4.3, it would appear that ion neutralization could possibly represent a substantial contribution to the substrate heat load. Self-bias voltage is important in thin film deposition as it determined the potential achieved by an isolated substrate. Effectively, the substrate will be bombarded by a flux of ions with energy approximately given by the product of their charge and the voltage difference between the self-bias and plasma potentials. This is also accompanied by an equal flux of electrons. It is seen that the initial rate of temperature rise decreases as the plasma density decreases. The photographs in Sect.4.8 (Figs.32) illustrate the effect of varying the resistance path to earth. It is quite clear that the plasma radiation intensity changes, accompanied by variations in species distributions. In view of these facts, it is not unreasonable to assume that ion bombardment effects influence the substrate heat load.

### 5.3 ANALYSIS of FILM STRUCTURE

For microstructure analysis, the film samples were prepared as previously discussed, and studied with the assistance and guidance of Mr.J.S. Bates on a JEOL JEM 100 CX transmission electron microscope.

The position of the rings on the diffraction patterns can provide information on the crystal structure of the films. The radii of these rings were obtained from the negatives. The ring radius  $r$  is related to the

crystal plane separation  $d$  by:  $d = \lambda L/r$ , where  $\lambda$  is the de Broglie wavelength of the matter waves associated with electrons and  $L$  is the camera length. These were  $0.037 \times 10^{-10} \text{ m}$  and  $0.731 \text{ m}$  respectively. Table 3. in Sect.4.4 summarizes the data obtained and lists the crystal plane separations of hexagonal-close-packed (HCP) and face-centred-cubic (FCC) Cobalt from the ASTM index for comparison with those calculated for the deposited films.

Fig.25 shows the diffraction patterns obtained for a range of self-bias voltage. The patterns, though faint, indicate that the films are polycrystalline; the granular/spotty rings characteristic of this were more evident on the negatives under illumination on a light-table. Films of thickness 100 nm were used for these analyses. The thermal conductivities of glass and mica are similar, thus the nature of the interfacial layer with respect to substrate temperature should not show substantial variation between the two cases. The use of mica substrates for film structure analyses is a generally accepted technique (5). The films analyzed by TEM experienced problems with resolution. The deposited films exhibit a reasonable packing density, nevertheless, films less than 200 nm in thickness should produce well defined diffraction patterns. It is possible that as the films are magnetic, the operation of the TEM facility was influenced. With regard to the phase content of the films, it is seen that a mixture of HCP and FCC phases are present in the films. From this observation it would seem that Cobalt transforms from the HCP phase to the FCC phase at relatively low temperatures. The substrate heat load analysis indicating that the maximum substrate temperature was  $200^{\circ} \text{ C}$ . However, there is evidence (6) that the surface temperature may be much higher than the measured probe temperature. The FCC phase corresponds to a low anisotropy, this has consequences for the existence of a preferred crystal



orientation and for the magnetic properties of the film.

The images exhibit different intensities in the ring patterns. This might imply some preferred crystal orientation, however, the image recording processes are non-linear and no calibration from which the true intensities could be derived was available. The crystal plane separations exhibit two notable features. A ring corresponding to the (1,0,0) plane of HCP Cobalt was expected, i.e.  $d = 2.165 \times 10^{-10}$  m. This absence may be accounted for by the presence of the FCC components, and that the intensity of this ring is expected to be a fifth of the ring for  $d = 1.91 \times 10^{-10}$  m. Having already illustrated the difficulty experienced with TEM resolution, it is not too surprising that this ring is not seen. Moreover, the experimental ring  $d = 1.37 \times 10^{-10}$  m did not correspond to any plane separation given in the ASTM index for Cobalt. However, EDAX compositional analysis revealed a presence of an Iron content of around 7% in all the films. It is likely that this ring is due to Iron or one of its oxides.

The bright-field images also suffered from TEM resolution problems. Only generalizations may be drawn from these images, Sect.4.4 and Figs.26. The images indicate a fairly densely packed structure with small crystal sizes, less than 100 nm. However, in the opinion of Mr.J.S. Bates who performed the TEM analysis, the crystal size appears to pass through a maximum and then decrease for increasing self-bias voltage. The maximum crystal size occurring for a self-bias voltage of around -25 V. An attempt to estimate the crystal size by X-ray diffraction techniques were unsuccessful due to the difficulty of reliably interpreting the results. The film thickness was such that the instrument electronics could not distinguish between scattered radiation and background noise. It is improbable that the grains are spherical, as they should exhibit some growth perpendicular to the film

plane. An estimate of the crystal size was obtained by preparing a 1 mm grid using photoreduction and determining a grain size distribution under magnification. Samples of fifty grains were taken, however, this method is subjective and only intended to provide an estimate. Fig.27 Sect.4.4 illustrates the observed distributions. They appear to be in reasonable agreement with the observations of Mr.J.S. Bates.

The diffraction patterns indicate the presence of HCP and FCC phases of Cobalt. The existence of a preferred orientation cannot be established. A preferred orientation, corresponding to an uniaxial anisotropy normal to the film plane of Cobalt, would be expected to manifest itself as a decrease in the (0,0,2) diffraction intensity. Other diffractions such as (1,1,0) and (1,0,0) which are vertical to the (0,0,1) basal plane should increase in intensity as a result. As previously explained, the imaging processes were non-linear and no calibration was available. Moreover, this precludes estimation of FCC content since the ring intensity should increase with FCC content as well as with increase in temperature.

The bright-field images would seem to indicate grains of sizes 10 nm to 50 nm surrounded by a densely packed array of smaller particles. The films would thus appear to consist of Cobalt particles, whose large anisotropy constant is responsible for the magnetic properties, embedded in a background of either amorphous or superparamagnetic Cobalt particles, or a combination of the two. This view of the film composition does not conflict with the evidence obtained from the diffraction patterns or the X-ray diffraction method. The TEM diffraction pattern of a crystalline film would exhibit rings of well defined spots, whereas an amorphous film would exhibit broad rings. The X-ray diffraction patterns would produce large peaks at angles of  $30^{\circ}$  to  $45^{\circ}$ , or nothing above background in the respective cases.

The observed pattern was more of a broad rise somewhat above background with what appeared to be peaks superimposed.

Cross-sections of the film samples were examined by TEM after ion beam milling. The resolution was poor but the images did reveal some information. The microstructure for films of thickness 550 nm, grown for the case of an earthed anode (the balanced magnetron case Fig.28), exhibit a growth habit perpendicular to the film plane that is akin to the columnar structure of crystalline films as given in the zone model of Movchan and Demischin. This growth habit is probably due to surface roughness and geometric shadowing, with the film building up in the preferred evolutionary direction dictated by these factors. The image indicates that this structure has these columns separated by regions devoid of material. It is possible that these empty regions influence the coercivity of the material. Cross-sections for the films deposited under increasing bias are not included for comparison because they proved too difficult to obtain images for. However, under observations by TEM in the opinion of Mr.J.S. Bates, the columnar/empty region structure appeared to exhibit smaller widths between the columns as self-bias increased. At larger biases they seemed to disappear altogether.

This could possibly be explained in terms of incident ion energies. For bulk Cobalt the adatom bond strength is about 1.74 eV (7), thin film values are unlikely to exceed this to any great extent (8). It is known that adatom mobility increases with ion bombarding energy (9). In the experimental case, the larger the ion energy the greater the transfer fraction of its kinetic energy (by momentum) to the growing film. It is possible that this process could lead to structural rearrangements of the film.

The parameter  $T/T_m$  may be used as an indicator to events occurring during film growth, similar to its use in the zone model as previously discussed. From the heat load measurements, for resistances to earth of  $3\ \Omega$ ,  $20\ \Omega$  and infinity, the respective  $T/T_m$  values are 0.21, 0.23, 0.27. It is possible that at higher  $T/T_m$  adatom mobility is sufficient to overcome the effects of geometric shadowing. This would perhaps lead to a more closely packed structure of small particles. It is observed that for larger biases, the particle sizes are at the lower end of the given range. The substrate temperature is an important parameter when considering the nature of thin film growth. During growth a hot absorption layer is present just above the condensing surface where the sputtered atoms and plasma species reach the surface (10). The influence of ion bombarding energy on this layer has yet to be investigated.

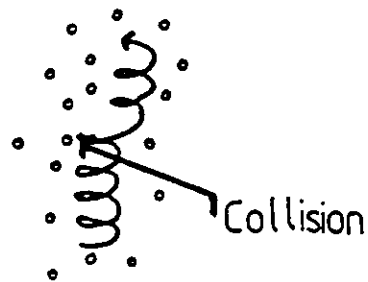
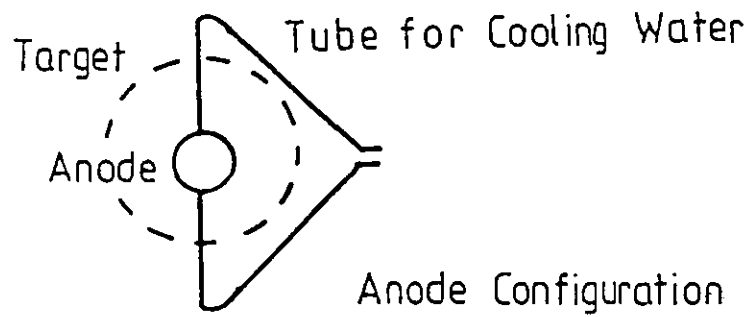
#### 5.4 SELF-BIAS and PLASMA MEASUREMENTS

The discharge in the given magnetron configuration is confined in the magnetic tunnel defined by the cathode surface and the surface defined by the last field line that intersects the anode surface. The magnetic field at the anode should act as a magnetic mirror and should reflect approaching electrons back towards the magnetron pole. Collisions will ensure, and they will move away from the axis towards the anode and chamber walls. This will produce an electron flux to the substrate, i.e. it will charge negatively.

The figure in Sect.4.1 illustrates the calibration of self-bias voltage at the substrate  $V_f$  and anode  $V_a$  versus the resistance to earth  $R$ . The case  $R = \text{infinity}$  occurs when the anode is disconnected from the box, i.e. it is floating.

The case for a floating anode leads to an intense plasma beam to the substrate, see Figs. 32 in Sect.4.3. When the anode is earthed, the balanced magnetron condition, the plasma is mainly confined to the cathode region. Altering the resistance to earth disturbs the plasma and it becomes unbalanced. The particle distributions are considerably different compared to the balanced case, as evidenced by the photographs in Sect.4.3. These photographs illustrate the effect of the resistance to earth on the nature of the plasma beam. For  $R > 20 \Omega$  or so, there is little visual difference in the appearance of the plasma beam. Beam confinement to the substrate increases as  $R$  increases. this effectively alters the plasma beam volume and hence the particle densities. It is to be expected that the maximum self-bias voltage attainable, limited by the magnetic configuration of the system, would occur for the case  $R = \text{infinity}$ . This is not seen in table 2, although  $V_f$  appears to be approximately constant for  $R > 20 \Omega$ . As given in Sect.4.3 the particle distributions around the probe may account for this discrepancy and obscure the true variation of  $V_f$ . Note that no quantitative information relating to the plasma distributions was obtained.

Fig.34 illustrates the variation of substrate self-bias across the central region of the substrate position. It is seen that the distribution is not symmetrical. Apart from the nature of the electron flux already discussed, two other factors are worthy of note. Firstly, there is an anode masking the target, 30 mm from the target (Fig.33). It is possible that particle distributions and magnetic field lines could be distorted by the shape of the anode. Secondly, the pump vent port is situated to one side of the substrate position. This could lead to a gas pressure gradient in the chamber, which could influence plasma characteristics.



Electron motion due  
to collision

Fig 33 Illustration of anode  
masking of target

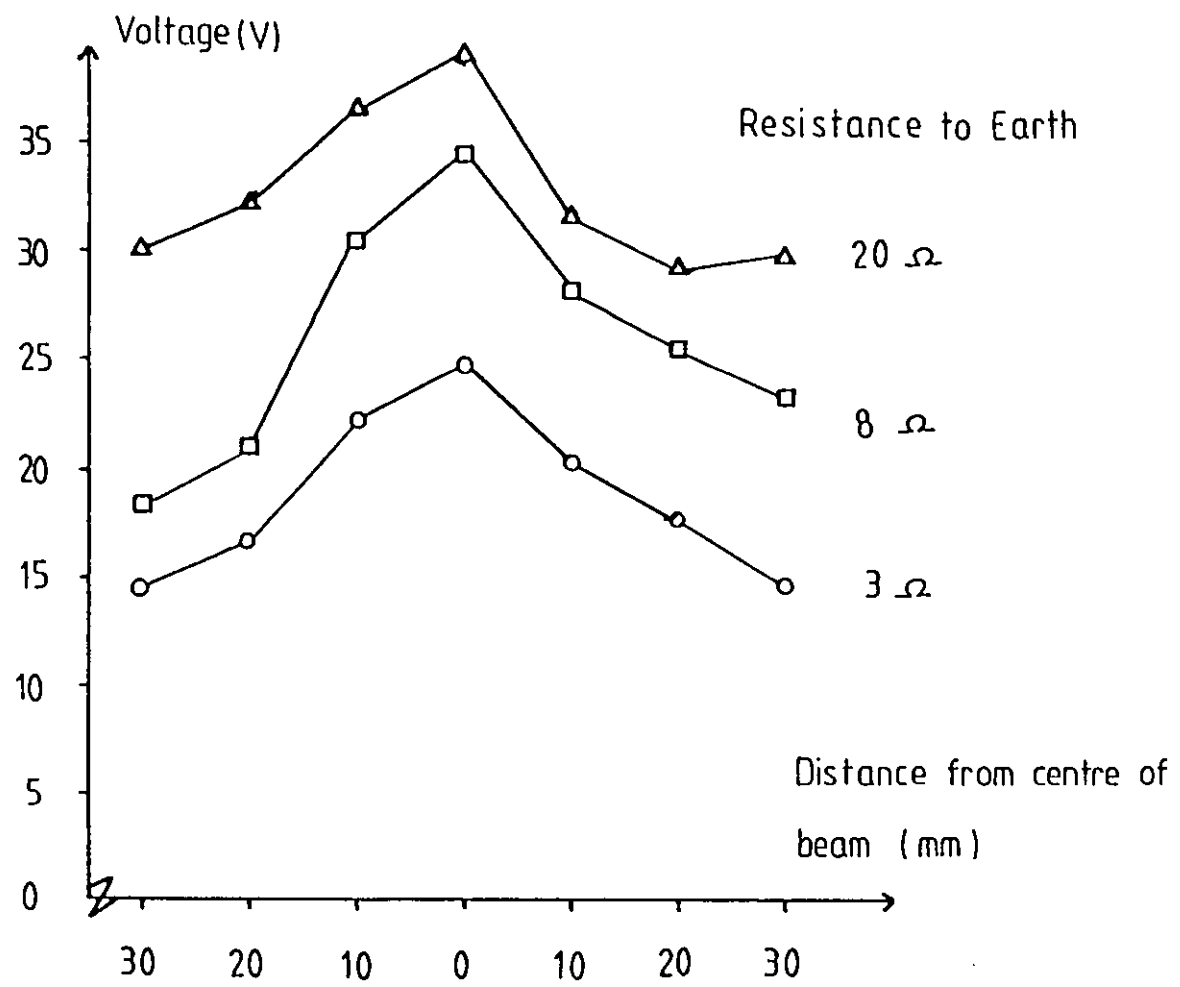


Fig34 Self Bias variation with position

The magnetic field configuration in the chamber may be used to support some of the observations made. As the contour map indicated, parallel lines of constant field exist near the substrate position. This leads to low fluxes as electron mobility across a field line is low. This would support the above observations relating to the variation of self-bias across the substrate. Another implication is that the electron flux away from the centre of the target must decrease, hence, so must the ion flux to the substrate. The observed variation in the film properties confirms that to obtain optimum film properties, the substrates must be located in the centre of the plasma beam along the magnetron axis.

The plasma parameters measured were the ion saturation current and substrate self-bias voltage. Portions of the current-voltage characteristics were also measured. The equations given in Sect.4.3 were used to determine other parameters such as electron temperature, species density and the Debye length. It proved difficult to measure the electron current in the accelerating region of the curve. The large current in this region leads to electron avalanche and thus the measurements made were unreliable. Moreover, the sensitivity of the method used to determine the probe characteristics was limited. It proved impossible to adequately investigate the region of the curve from probe voltages of -1 V to positive voltages. As discussed in Sect.4.3, a bimodal electron distribution is normal for the magnetron conditions employed for film deposition. The presence of such could not be detected, thus its existence could not be confirmed. The conventional parameter accepted as the electron temperature  $T_e$  was calculated from the measurements made. For the case of a floating anode, the electron temperature was higher than that for other bias conditions. For this condition, the plasma beam to the substrate was intense. Measurements made under such conditions would most likely be severely disturbed. The



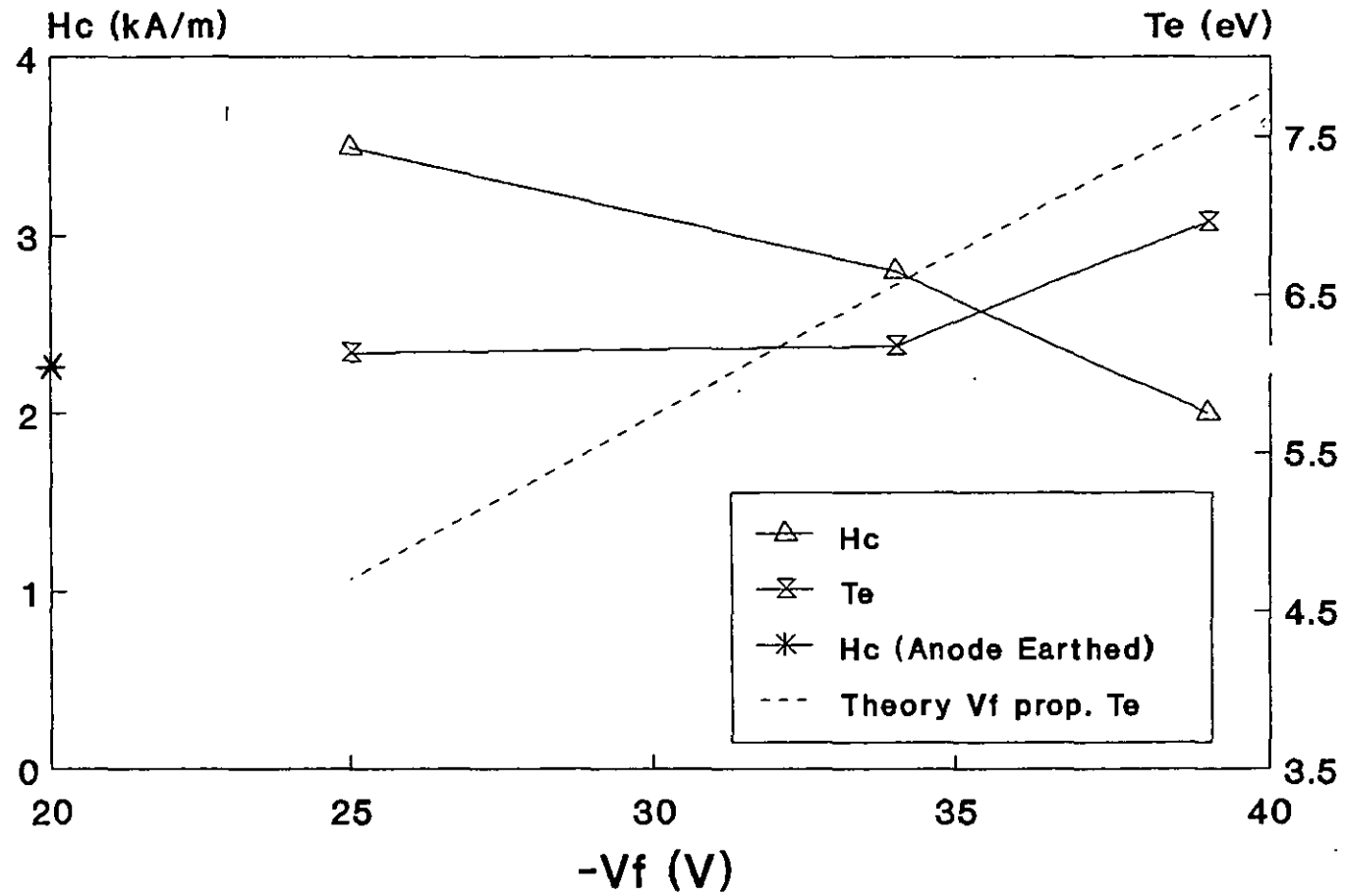
self-bias voltage does not appear to follow the linear relation in Sect.2.4. This is not expected, since the assumptions on which it is based do not rigorously apply in the experimental case. Fig.35 shows the variation of  $T_e$  with substrate self-bias for the experimental case, with the theoretical curve included for comparison.

A few more observations from the plasma data are worth noting. The Debye lengths  $\lambda_d$ , calculated from the electron temperature, lead to values that are in accordance with the assumption that the probe radius is greater than  $\lambda_d$ . The plasma density,  $n_p$ , increases with increasing resistance to earth since  $n_p$  is proportional to  $n_{es}$ . This may also be seen in the photographs of Sect.4.3. The probe current for a probe voltage of +1 V was measured in order to obtain some estimate for the electron saturation current. It is seen that it is of the order 100 to 500 mA for the various cases. As stated, this portion of the characteristics could not be adequately measured. Although the power rating of the precision resistor was 10 W, the resistor was found to heat rapidly when measurements in this region were attempted. The plasma potential was not directly measured. However, as a rough estimate, based on extrapolation of the probe characteristics, a value of +2 V for  $V_p$  was found. This is consistent for low pressure plasmas of the type used under the given conditions (1). The plasma potential is generally accepted to be within a few volts of zero.

## 5.5 MAGNETIC MEASUREMENTS

Measurements were attempted with a vibrating sample magnetometer of the Foner type. However, the instrument sensitivity proved to be insufficient to measure the in-plane coercivities. The saturation magnetism and remanence could not be determined by this method either. The instrument

Fig 35 Electron Temperature and Coercivity versus Substrate Self Bias



operation appeared to be impaired when attempting to analyze the film samples. A possible reason for this could have been that the direction of magnetism was not in the plane of the film. However, the technique of using Bitter patterns to observe the domain configurations did not reveal any evidence to support this idea. Moreover, it was established earlier that no preferred orientation could be detected. The apparatus used to measure the in-plane film coercivities is described in Sect.3.9. As stated there, the vertical hysteresis loop axis is calibrated in arbitrary units. No information or measurement of the saturation magnetization and remanence could be obtained. The only magnetic property of the films that could be investigated was that of their coercivity.

The figures in Sect.4.6 illustrate the hysteresis loops of films deposited under a range of self-bias. For the case of a floating probe, the coercivity  $H_c$  is low, about  $1.8 \text{ kAm}^{-1}$ . This appears to be related to the deposition conditions of low Argon gas pressure and a relatively high substrate temperature. Moreover, the cross-section of this film exhibited little or no voiding, while the bright-field image appears to show a densely packed film. It is possible that particle interactions could be responsible for this low value of coercivity.

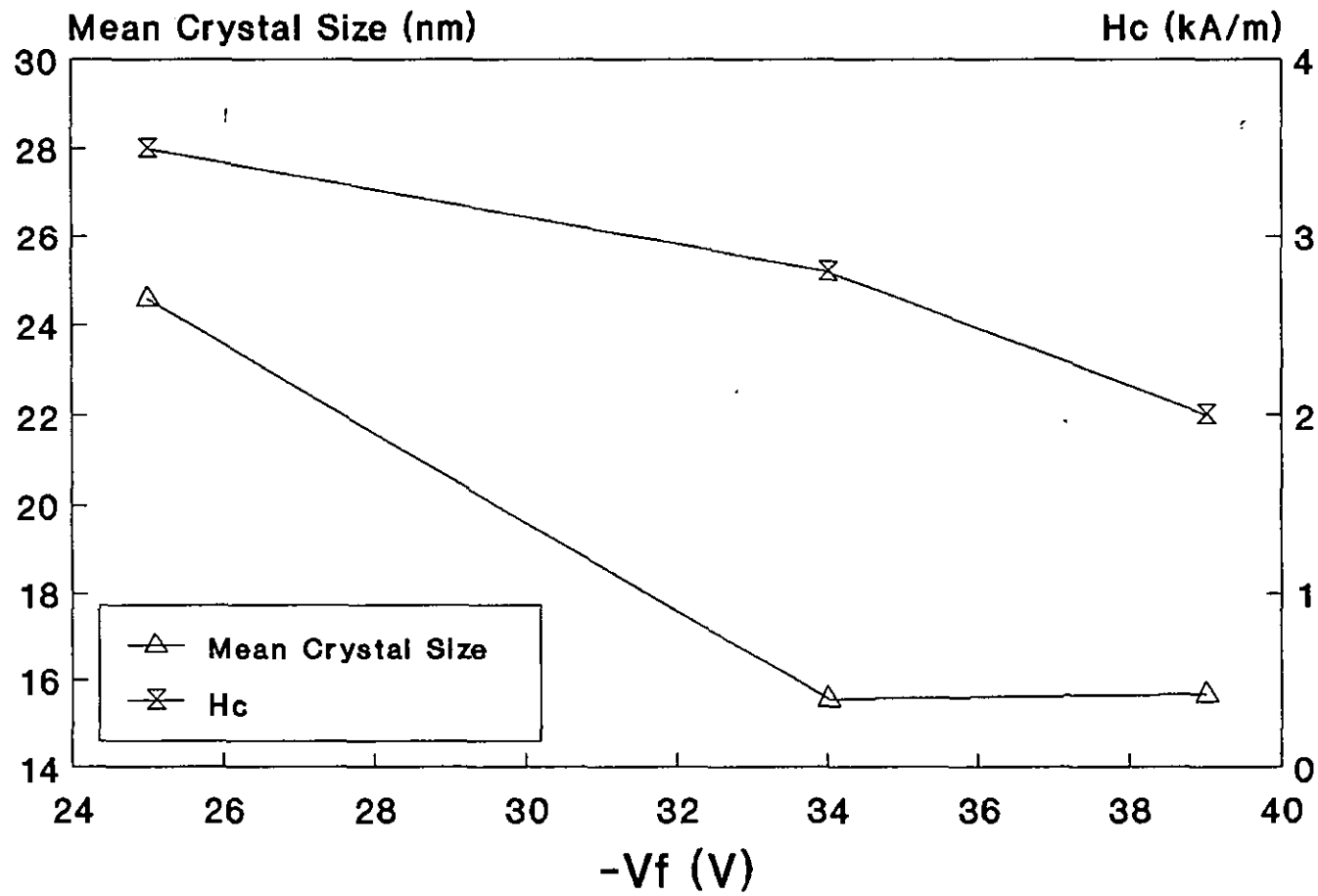
The figures illustrate a marked variation in coercivity with substrate self-bias. It appears that the coercivity decreases as the film bias increases. No films were prepared for a bias in the range 0 to -20V. It is not reasonable to categorically state that the coercivity achieved a maximum bias. However, the coercivity would appear to exhibit a maximum in the range 0 to -25 V self-bias.

The crystallite sizes for the floating anode cases are small,  $\leq 10$  nm. This combined with little or no apparent voiding in the film would suggest that particle interactions could account for the low observed coercivity of the films. For the films exhibiting voiding, the coercivity is larger than for those without. This also indicates that particle interactions, for a more densely packed structure, influence the film coercivity. As self-bias increases so the voiding width appears to decrease, as does the crystallite size. Fig.36 illustrates the variation of coercivity with film self-bias. The crystal size distributions appear to indicate that the largest crystallite size coincides with the largest observed coercivity. This is in agreement with the theoretical and experimental data of Luborsky (18) obtained for Iron and Cobalt. The deposited films yield a coercivity maximum of  $3.5 \text{ kAm}^{-1}$  for particle diameters in the range 20 to 30 nm.

The behaviour of small magnetic particles depends upon their sizes. As the size decreases, the magnetic behaviour of the particles changes. As the size reduces, behaviour goes firstly from multi-domain to single-domain, and upon further reduction from single-domain to superparamagnetic (11).

If the wall energy of Cobalt is taken as  $3 \times 10^{-3} \text{ Jm}^{-3}$  and  $M_s$  as  $1.79 \text{ Wbm}^{-2}$ , then the size for superparamagnetic particles is approximately 7.6 nm (12). The critical size for single domain particles is around 42 nm (12). The crystal size (d) range for superparamagnetic to single-domain particle is  $8 \text{ nm} < d < 42 \text{ nm}$ . The crystal size distributions for the deposited films lie in this range. The earlier mentioned view of the film as consisting of Cobalt particles in an amorphous and/or superparamagnetic background is thus a reasonable proposition. The coercivity of bulk Cobalt is  $0.797 \text{ kAm}^{-1}$  (13). The deposited films all exhibit a value larger than this. For films deposited without bias the coercivities agree with those of Kohmoto and

Fig 36 Crystal Size and Coercivity  
versus Substrate Self Bias



Yamamoto (14) who found a coercivity of  $2 \text{ kAm}^{-1}$  for films 300 nm thick at an Argon gas pressure of 0.5 Pa.

The possible relation between magnetic properties and microstructure of Cobalt thin films has been little investigated. Chen and Charlan (15) reported such a connection for films of thickness 10 to 170 nm. The observations of columnar type growth and empty regions in the deposited films is in reasonable accord with their observations by TEM. The effect of self-bias, so far as can be ascertained, has not been elsewhere investigated. However, in the case of direct application of bias to a growing film, Okhoshi and Kusuda (16) found that for Cobalt-Chromium (CoCr) films both crystal size and magnetic properties could be influenced by bias. The trends observed in the deposited films, that is the possibility of influencing the values of crystal size and film coercivity by control of film self-bias, concur with their findings for CoCr.

## 5.6 FILM STRESS

There are two main components of film stress, intrinsic and thermal. Thermal stress results from the difference in the thermal expansion coefficients of the film and the substrate. Intrinsic stress is due to relative displacements of atoms and interatomic forces.

No measurements were performed but some observations may be noted. Films deposited on substrates that were not cleaned (using a glow discharge) appeared to be highly stressed and exhibited poor adhesion. This was noted whilst preparing samples for magnetic measurements. Upon cutting the glass substrate, the film curled away from the cut. This is an indication of tensile stress. The observed microstructure may be used to provide an

insight to film stress. Under low adatom mobility, empty regions interspersed the columnar type structure of the films. These defects may well exert an attractive interatomic force which would lead to a net tensile stress. Stress is known to be affected by substrate temperature and ion bombardment (17). There is strong evidence to suggest that ion bombardment has a direct influence on film stress via a modification of film microstructure by momentum transfer from incident species, and through re-sputtering of absorbed impurities.

## 5. REFERENCES

- 1) Oka K. and Howson R.P., C.E.P. Consultants, Edinburgh, U.K., (1987), p.158.
- 2) Window B. and Savvides N.J., J.Vac. Sci. Technol., A4 (2), (1986), p.196.
- 3) TU Y.Y., Chuang T.J. and Winters H.F., Phys. Rev., B23, (1981), p.823.
- 4) Lav S.S, Mills R.H. and Muth D.G., J.Vac. Sci. Technol., 9 (1972), p.1196.
- 5) Lodder J.C., Wielinga T. and Worst J., Thin Solid Films, 101, (1983), p.61-73.
- 6) Iwasaki S. and Ouchi K., Dig. 4<sup>th</sup> Ann. Conf. on Mag. Japan, Paper 6a, A4 (1980).
- 7) CRC Handbook of Physics and Chemistry, ed. Weast R.C., 62<sup>nd</sup> Ed. (1982), CRC Press, Inc. Boca Raton, Florida.
- 8) Thornton J.A., J.Vac. Sci. Technol., 15 (1978), p.188.
- 9) Thornton J.A., Ann. Rev. Mat. Sci., 7 (1977), p.239.
- 10) Sears C.W. and Cahn J.W., J.Chem. Phys., 33 (1960), p.494.
- 11) Cullity B.D., in Introduction to Magnetic Materials, Addison-Wesley, London (1972).
- 12) Kittel C., Phys Rev., 70 (1946), p.965.
- 13) Bozorth R.M., in Ferromagnetism, D.Van Nostrand, New Jersey (1955).
- 14) Kohmoto O. and Yamamoto T., J.Mag. and Magn. Mat., 71 (1987), p.33.
- 15) Chenn T. and Charlan G.B., J.Appl. Phys., 50 (1979), p.4285.
- 16) Okhoshi M. and Kusuda T., J.Vac. Sci. Technol., A5 (5) (1987), p.2589.
- 17) Cuomo J.J., Harper J.M.E., Guarnieri C.R., Yee D.S., Attanasio L.J., Angiello J. and Wu C.T., J.Vac. Sci. Technol., 20 (1982), p.349.
- 18) Kneller E.F. and Luborsky F.E., J.Vac. Sci. Technol., 34 (1963), p.656.



## **6.CONCLUSIONS**

The deposited films contained a mixture of FCC and HCP phases. The FCC content is consistent with a low temperature phase change. This effect may have been induced by substrate heating. The presence of the FCC phase reduces the uniaxial crystal anisotropy, thereby reducing the coercivity. No preferred crystal orientation for the films could be detected.

The power supplied to the system is mainly dissipated as heat at the target and anode. Of the supplied power absorbed as heat at the substrate, a significant fraction is contributed by ion neutralization.

Self-bias and the attendant ion bombardment influence the both the microstructure and properties of deposited films. The effects are controllable and reproducible under the given experimental conditions.

Self-bias is seen to influence the coercivity and particle size of the films. A maximum in the film coercivity is seen to coincide with a maximum in the film crystallite particle diameter. Theoretically, the maximum coercivity of Cobalt should lie in a crystallite diameter range of  $7.6 \text{ nm} < d < 42 \text{ nm}$ . This is the range for single-domain particles. The deposited films ranged in diameter from 10 nm to 35 nm. This implies that the the films probably contain a large number of single-domain particles.

Analogous known zone models, void width and particle interactions may be used to explain the variation of film coercivity and crystallite diameter with self-bias. Increasing the self-bias decreases the crystallite diameter and void width. The film coercivity decreases probably as a result of greater packing fraction and particle interactions within the films.

The deposited films are probably composites of single-domain particles randomly oriented in a background of superparamagnetic particles and/or amorphous Cobalt. The observed properties of the magnetic films are probably due to the anisotropic nature of these single-domain particles.

